J. Fluid Mech. (2024), *vol*. 999, A28, doi:10.1017/jfm.2024.640

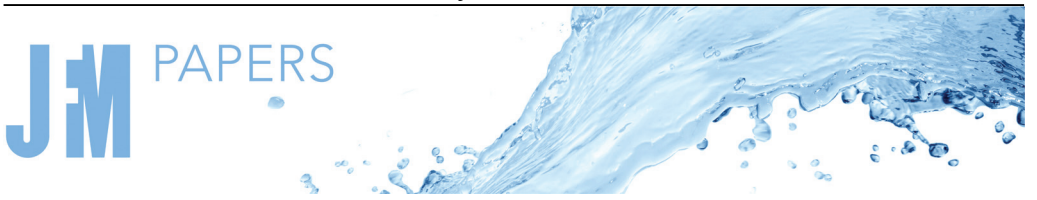

Turbulent convection in rotating slender cells

Ambrish Pandey[1,2,†] **and Katepalli R. Sreenivasan**[2,3]

[1]Department of Physics, Indian Institute of Technology Roorkee, Roorkee 247667, Uttarakhand, India

[2]Center for Astrophysics and Space Science, New York University Abu Dhabi, Abu Dhabi 129188, UAE

[3]Tandon School of Engineering, Department of Physics, and Courant Institute of Mathematical Sciences, New York University, New York, NY 11201, USA

(Received 17 February 2023; revised 18 June 2024; accepted 18 June 2024)

Turbulent convection in the interiors of the Sun and the Earth occurs at high Rayleigh numbers Ra, low Prandtl numbers Pr, and different levels of rotation rates. To understand the combined effects better, we study rotating turbulent convection for $Pr = 0.021$ (for which some laboratory data corresponding to liquid metals are available), and varying Rossby numbers Ro, using direct numerical simulations in a slender cylinder of aspect ratio 0.1; this confinement allows us to attain high enough Rayleigh numbers. We are motivated by the earlier finding in the absence of rotation that heat transport at high enough Ra is similar between confined and extended domains. We make comparisons with higher aspect ratio data where possible. We study the effects of rotation on the global transport of heat and momentum as well as flow structures (*a*) for increasing rotation at a few fixed values of Ra, and (*b*) for increasing Ra (up to 10^{10}) at the fixed, low Ekman number 1.45×10^{-6}. We compare the results with those from unity Pr simulations for the same range of Ra and Ro, and with the non-rotating case over the same range of Ra and low Pr. We find that the effects of rotation diminish with increasing Ra. These results and comparison studies suggest that for high enough Ra, rotation alters convective flows in a similar manner for small and large aspect ratios, so useful insights on the effects of high thermal forcing on convection can be obtained by considering slender domains.

Key words: Bénard convection, rotating flows, turbulent convection

1. Introduction

Convection in most natural settings, such as the Earth's interior and Jupiter's atmosphere (Heimpel, Aurnou & Wicht 2005), and the interior convection of the Sun (Hanasoge,

† Email address for correspondence: ambrishiitk@gmail.com

Gizon & Sreenivasan 2016), coexists with rotation. Rotating Rayleigh–Bénard convection (RRBC), where a fluid layer rotates uniformly about its vertical axis and is simultaneously heated from the bottom and cooled from the top, is a popular model of such flows (Ecke & Shishkina 2023). The characteristics of RRBC depend on the Prandtl number Pr (the ratio of the heat and momentum diffusion time scales), the Rayleigh number Ra (the ratio of the buoyancy force to effects of thermal diffusivity and viscosity of the fluid), and the Ekman number Ek (the time scale ratio of rotation and momentum diffusion). The Prandtl number is small in many natural convective flows: $Pr \sim 0.01$–0.1 in the Earth's outer core (Aurnou *et al.* 2015; Pandey *et al.* 2022*b*), and $Pr \sim 10^{-6}$ in the Sun's interior (Schumacher & Sreenivasan 2020). Despite the importance of the low-Pr RRBC, and the awareness that it is distinct from convection at moderate and high Pr (King & Aurnou 2013; Horn & Schmid 2017; Aurnou *et al.* 2018), it has not been explored as extensively as its high-Pr counterpart. In this paper, we study RRBC at the low Pr value 0.021 for a range of rotation rates, with the Ra range that includes the onset of convection as well as the turbulent state.

To optimize computational resources (see also the discussion at the end of § 2), we use a cylindrical domain of aspect ratio $\Gamma = 0.1$. Here, Γ is the diameter to height ratio of the cell. We demonstrated recently (Pandey & Sreenivasan 2021; Pandey *et al.* 2022*a*) that many properties of convective flows in the slender cell are similar, in the absence of rotation, to those in extended domains of $\Gamma = 25$, when Ra is large. Similarly, while the flow structures near the onset of convection indeed depend on Γ, they may be expected to be similar between confined and extended domains if Ra is large. In any case, wherever possible, we make explicit comparisons with data from wider convection cells. Note, however, that directional confinement has been observed to alter the flow properties in different ways in Rayleigh–Bénard convection (RBC) depending on the control parameters (Wagner & Shishkina 2013; Chong *et al.* 2015; Chong & Xia 2016). For example, Chong *et al.* (2015) found for $Pr = 4.38$ that in rectangular domains of dimensions (H, L_y, H), the heat transport gets amplified and attains a maximum when $\Gamma_y = L_y/H$ decreases, and reaches a certain Ra-dependent critical Γ_y. The narrower boxes, however, were observed to become increasingly resistant to the momentum transport. On the other hand, Wagner & Shishkina (2013) observed for $Pr = 0.786$ that both the heat and momentum transports generally decrease when Γ_y is changed from 1 to $1/10$.

For comparison purposes, we also perform the direct numerical simulations (DNS) of convection in rapidly rotating and non-rotating cells for the same range of Ra, while maintaining Pr low at 0.021. We study the effects of rotation on flow structures as well as global heat and momentum transports. Specifically, we consider the following.

(1) The effect of rotation on the critical Rayleigh number Ra_c. We elucidate the change in the large structure of the flow, in particular the evolution of the organized helical structure at low Ra into one with increasing small-scale content.

(2) The effect of rotation near the onset of instability. For horizontally unbounded rotating layers, linear stability theories show that the onset of convection is delayed in Ra, with the critical Rayleigh number Ra_c and the corresponding length scale ℓ_c depending only on Ek when Pr is moderate and large (Chandrasekhar 1981). For low Pr as well, the dependence of onset parameters on Pr is known explicitly (Chandrasekhar 1981; Zhang & Liao 2017). What is not known is the behaviour of the heat transport for low Pr. For moderate Pr, the excess heat transport (Ecke & Niemela 2014; Plumley & Julien 2019; Kunnen 2021) given by $Nu - 1$ increases linearly with the supercriticality $\epsilon = Ra/Ra_c - 1$ (Gillet & Jones 2006; Ecke 2015; Long *et al.* 2020) – the Nusselt number Nu being the ratio

of the actual heat transport to that enabled by conduction alone – but the corresponding behaviour of low Pr has not yet been explored.

(3) The scaling of heat and momentum transport for large Ra range. A range of scaling exponents β in the empirical relations $Nu \sim Ra^{\beta}$ has been observed in RRBC. In the rapidly rotating regime, β is as large as 3.6 for convection in water, with β decreasing as rotation decreases (King *et al.* 2009; King, Stellmach & Aurnou 2012; Cheng *et al.* 2015). Asymptotic simulations of RRBC have revealed that the heat transport scales as $Nu - 1 = Ra^{3/2}\, Pr^{-1/2}\, Ek^{2}$ in the geostrophic regime (Julien *et al.* 2012*a*; Aurnou, Horn & Julien 2020; Kunnen 2021). In rotating liquid gallium ($Pr \approx 0.025$), King & Aurnou (2013) reported β values varying from 0.1 to 1.2 in the rotationally influenced regime in a cylindrical cell with $\Gamma \approx 2$, while Aurnou *et al.* (2018) found $\beta \approx 0.9$ for a similar aspect ratio ($\Gamma = 1.9$). We examine the validity of these expectations.

(4) The bulk temperature gradient in the rotating slender cells. The inhibition of turbulent mixing by rotation is often manifested by the presence of significant vertical temperature gradient $\partial T/\partial z$ in the bulk region. This gradient varies non-monotonically in RRBC (Cheng *et al.* 2020; Aguirre Guzmán *et al.* 2022), and, for moderate Pr, the rapidity of its variation with Ra indicates various flow structures (Julien *et al.* 2012*b*). The low-Pr case has been restricted mostly to moderate Ra (King & Aurnou 2013; Horn & Schmid 2017; Aurnou *et al.* 2018; Aguirre Guzmán *et al.* 2022) because of numerical and experimental challenges (Pandey *et al.* 2022*b*). Here, we quantify $\partial T/\partial z$ in the bulk region in both low- and moderate-Pr convection, carrying out the DNS for high Ra, and find that it is qualitatively similar to that in wider cells.

(5) Viscous boundary layer near the horizontal plate. In non-rotating convection, the viscous boundary layer near the plates becomes thinner with increasing thermal forcing, whereas its width δ_u is determined by the Ekman number in RRBC; in rapidly rotating convective flows, $\delta_u \sim \sqrt{Ek}$ (King, Stellmach & Buffett 2013). We estimate δ_u and find that it scales as $\sqrt{Ek}$ in the rotating slender cells when rotation effects dominate the thermal forcing. We further compare the velocity profile in the near-wall region and observe very good agreement with the analytical Ekman layer profile (Aguirre Guzmán *et al.* 2022) in the regime where $\delta_u \sim \sqrt{Ek}$ scaling holds well.

As the onset length scale decreases with decreasing Ekman number, convective structures grow in number with decreasing Ek in a domain of fixed Γ. This aspect has been utilized by researchers by exploring rotating convection at low Ek (and high Ra) in slender convection domains because the effects of confinement may be rendered insignificant by the presence of a multitude of elementary flow structures (Cheng *et al.* 2015, 2018, 2020; Madonia *et al.* 2021). However, flow properties in confined RRBC domains could be altered in an intricate manner – for example by the so-called boundary zonal flow (Shishkina 2020; Zhang *et al.* 2020; Zhang, Ecke & Shishkina 2021; Ecke, Zhang & Shishkina 2022; Wedi *et al.* 2022) or sidewall circulation (Favier & Knobloch 2020; de Wit *et al.* 2020). In the present work, the slender convection cell contains between 1 and 3 elementary structures at the onset, clearly indicating that the flow is confined in that context. In spite of this, the way the flow is altered due to rotation is essentially the same as in flows in wider cells, especially at higher Ra.

After a brief discussion of the simulation tools in § 2, we present comments on flow morphology in § 3. Flow structures near the onset of convection are discussed in § 4, the scaling results on global heat transport in § 5, and the temperature gradient in the bulk region and the viscous boundary layer in § 6. A few concluding remarks are presented in § 7 while important parameters of our simulations are summarized in Appendix A.

2. Simulation methodology

We solve the non-dimensional Oberbeck–Boussinesq equations

$$\frac{\partial \boldsymbol{u}}{\partial t} + \boldsymbol{u}\cdot\boldsymbol{\nabla}\boldsymbol{u} = -\boldsymbol{\nabla} p + T\hat{z} - \frac{1}{Ro}\,\hat{z}\times\boldsymbol{u} + \sqrt{\frac{Pr}{Ra}}\,\nabla^2\boldsymbol{u}, \tag{2.1}$$

$$\frac{\partial T}{\partial t} + \boldsymbol{u}\cdot\boldsymbol{\nabla} T = \frac{1}{\sqrt{Pr\,Ra}}\,\nabla^2 T, \tag{2.2}$$

$$\boldsymbol{\nabla}\cdot\boldsymbol{u} = 0, \tag{2.3}$$

where $\boldsymbol{u}$ ($\equiv u_x\hat{x} + u_y\hat{y} + u_z\hat{z}$), T and p are the velocity, temperature and pressure fields, respectively. The normalizing length H is the height between the horizontal plates, and ΔT is the temperature difference between them. The free-fall velocity $u_f = \sqrt{\alpha g\,\Delta T\,H}$ and the free-fall time $t_f = H/u_f$ are the relevant velocity and time scales. The Rayleigh number is $Ra = \alpha g\,\Delta T\,H^3/(\nu\kappa)$, and the Prandtl number is $Pr = \nu/\kappa$. The convective Rossby number $Ro = u_f/(2\Omega H) = \alpha g\,\Delta T/(2\Omega u_f)$ is the ratio of the buoyancy and Coriolis forces, where Ω is the rotation rate, and α, ν, κ are the isobaric coefficient of thermal expansion, kinematic viscosity and thermal diffusivity of the fluid, respectively.

The simulations correspond to $Pr = 0.021$ and $2\times10^7 \le Ra \le 10^{10}$ in a cylindrical cell with $\Gamma = 0.1$ using the solver Nek5000, based on the spectral element method (Fischer 1997). The no-slip boundary condition is prescribed for the velocity field on all walls, and the isothermal and adiabatic conditions for the temperature field on the horizontal and sidewalls, respectively. The cylinder is decomposed into N_e elements, and the turbulence fields within each element are expanded using the Nth-order Lagrangian interpolation polynomials. Thus the number of mesh cells in the entire flow is N_eN^3; higher mesh density in the near-wall regions is used to capture rapid variations of the field variables. More details can be found in Scheel, Emran & Schumacher (2013), Iyer *et al.* (2020) and Pandey *et al.* (2022*a*). (Incidentally, the number of spectral elements N_e in Iyer *et al.* (2020) was 192 000 for $Ra = 10^8$, 10^9, 10^{10} and 10^{11}.)

The effects of rotation are studied using two different approaches. First, the effects of increasing thermal forcing are explored for a fixed $Ek = 1.45\times10^{-6}$ and varying Ra up to 10^{10}. The Ekman number $Ek = \nu/(2\Omega H^2)$ quantifies the strength of the viscous force relative to that of the Coriolis force, so we are dealing with a rapidly rotating case. Second, the effects of increasing rotation are studied by fixing $Ra = 10^8$, 10^9 and 10^{10}, and by decreasing the Rossby number for each Ra. Note that the convective Rossby number is also expressed as $Ro = Ek\sqrt{Ra/Pr}$; for a fixed Ra and Pr, Ek decreases with the decreasing Ro. The simulations for non-rotating convection serve as the reference state. To compare the flow properties with those of moderate-Pr convection, we additionally conduct RRBC simulations for $Pr = 1$ and Ra up to 10^{11}, but the emphasis in this paper is the low-Pr case. The parameter space in this study is shown in figure 1.

The Kolmogorov length scale is estimated as $\eta = (\nu^3/\varepsilon_u)^{1/4}$, where ε_u is the kinetic energy dissipation rate computed at each point in the flow as

$$\varepsilon_u(\boldsymbol{x}) = \frac{\nu}{2}\sum_{i,j}\left(\frac{\partial u_i}{\partial x_j} + \frac{\partial u_j}{\partial x_i}\right)^2, \tag{2.4}$$

where $i, j \equiv (x, y, z)$. To ensure the adequacy of the spatial resolution, we estimate the height-dependent Kolmogorov scale $\eta(z)$ using the area- and time-averaged dissipation rate $\langle\varepsilon_u\rangle_{A,t}(z)$, and ensure that the vertical grid spacing Δ_z remains of the order $\eta(z)$.

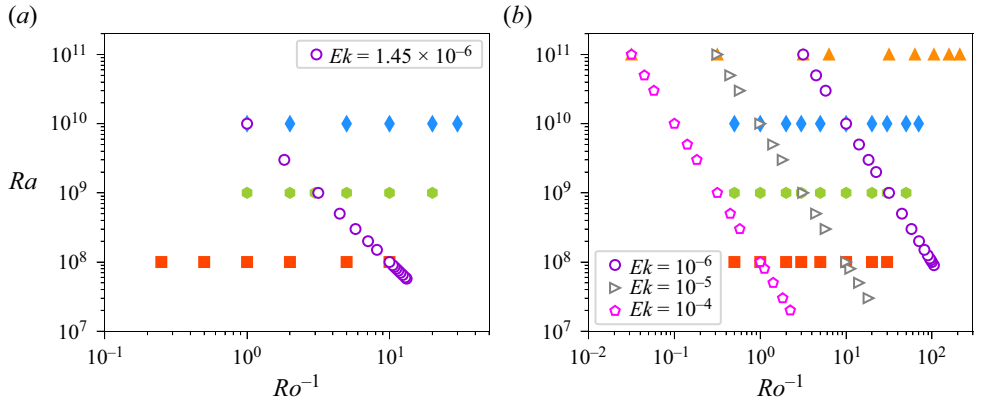

Figure 1. The parameter space explored in the present study for (*a*) $Pr = 0.021$ and (*b*) $Pr = 1$. Open symbols are for simulations with fixed rotation and varying thermal forcing, whereas filled ones are for simulations with fixed forcing and varying rotation rate. In (*a*,*b*), the sloping data are for variable *Ro* but constant *Ek*.

This constraint captures all significant variations in the velocity field. Further, within the Ekman layer, which varies as $\delta_u \sim \sqrt{Ek}$, we have embedded 5–20 grid points.

We briefly expand here on the computational gains in using a slender cell because the fluid volume is smaller by a factor of Γ^2. Higher *Ra* could thus be achieved for the same computational resources, compared to those of higher Γ. However, an increased fraction of fluid is affected by the sidewall, and the critical *Ra* for the onset of convection grows for small Γ (Shishkina 2021; Ahlers *et al.* 2022). To that extent, the computational advantage of using a slender domain to explore a highly turbulent regime of convection tends to be diminished, but one needs further exploration on these advantages in different Rayleigh number regimes.

3. Flow morphology

Multiple vertically stacked circulation rolls lead to helical structures in slender convection domains (Iyer *et al.* 2020; Zwirner, Tilgner & Shishkina 2020; Pandey & Sreenivasan 2021; Pandey *et al.* 2022*a*). The flow configuration in the non-rotating slender cell is shown in figure 2 for varying *Ra*. The instantaneous velocity streamlines shown in figures 2(*a–c*), coloured according to the vertical velocity, confirm the presence of vertically stacked rolls. The helical flow structure is relatively smooth for $Ra = 10^8$ (figure 2*a*) but becomes increasingly complex as the thermal forcing increases. The vertical velocity slices in figures 2(*d–f*) exhibit coherently moving flows, both up and down, with sizes comparable to the lateral extent of the flow. However, these organized structures incorporate increasingly smaller scales as *Ra* increases. The corresponding temperature isosurfaces in figures 2(*g–i*) show that the mixing is weak at low *Ra* but becomes increasingly effective as the thermal forcing becomes stronger. Even in a highly turbulent flow for $Ra = 10^{10}$ (figure 2*i*), a variety of temperature isosurfaces are present in the bulk region, which indicates that the turbulent mixing is weaker than in wider convection domains, where a well-mixed and isothermal bulk component is observed. The global heat transfer, however, is not very different in the two cases (Pandey *et al.* 2022*b*).

The critical parameters for the onset of non-rotating convection are independent of *Pr*. In contrast, the onset parameters in rotating convection do depend on the Prandtl number when it is less than 0.68 (Chandrasekhar 1981). Linear stability analysis for $Pr > 0.68$ in

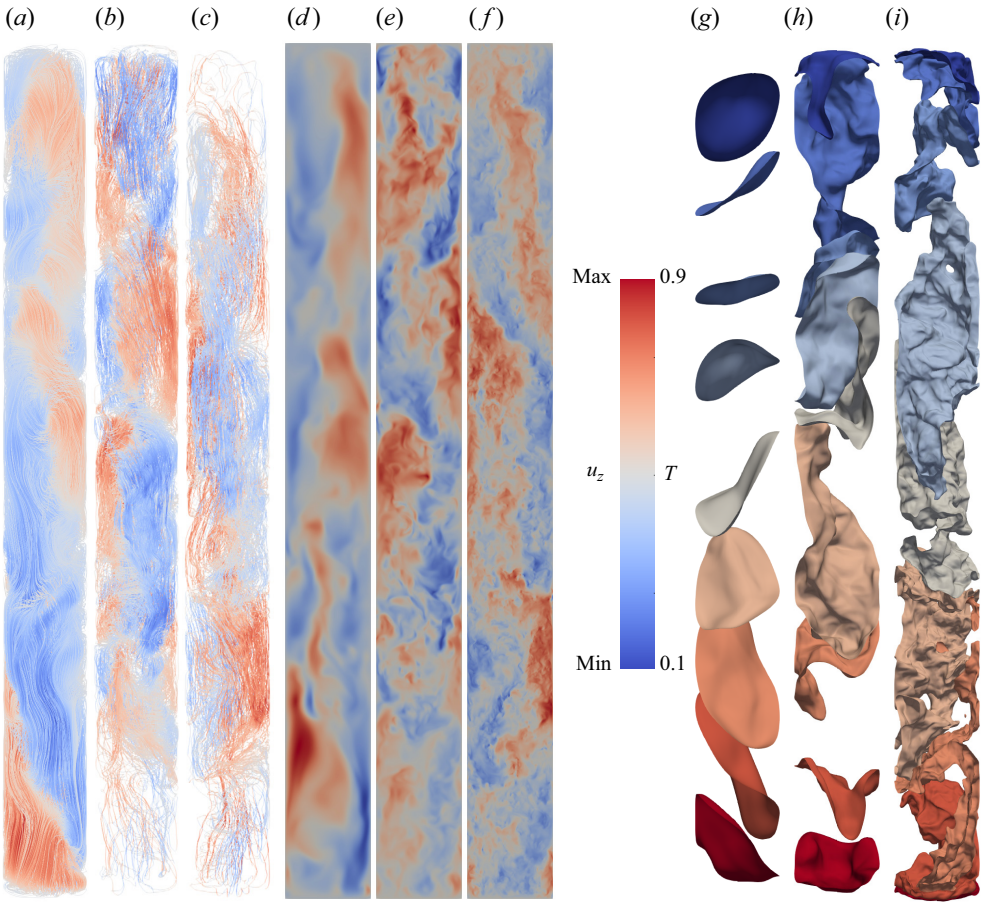

Figure 2. Instantaneous convective structures in a non-rotating slender cell for (*a*,*d*,*g*) $Pr = 0.021$ and $Ra = 10^8$, (*b*,*e*,*h*) $Ra = 10^9$, and (*c*,*f*,*i*) $Ra = 10^{10}$. The velocity streamlines (*a–c*), coloured by the vertical velocity, exhibit helical flow structures in the slender cell. Planar cuts of the vertical velocity (*d–f*) reveal that progressively finer flow structures are generated with increasing thermal forcing. Isosurfaces of the temperature (*g–i*) indicate that despite increased mixing with *Ra*, the isothermal bulk region, observed to exist in wider convection domains, is not present in the slender cell.

horizontally unconfined domains yields the Rayleigh number and the length scale for the steady onset as

$$Ra_c = 3(\pi^2/2)^{2/3}\, Ek^{-4/3} \approx 8.7\, Ek^{-4/3}, \tag{3.1}$$

$$\ell_c/H = (2\pi^4)^{1/6}\, Ek^{1/3} \approx 2.4\, Ek^{1/3}. \tag{3.2}$$

For low Prandtl numbers ($Pr < 0.68$), the critical parameters at the oscillatory onset depend on both *Ek* and *Pr* (Horn & Schmid 2017; Aurnou *et al.* 2018; Vogt, Horn & Aurnou 2021) as

$$Ra_c = 3\pi \left(\frac{2\pi}{1+Pr}\right)^{1/3} \left(\frac{Ek}{Pr}\right)^{-4/3}, \tag{3.3}$$

$$\ell_c/H = (2\pi^4)^{1/6}(1+Pr)^{1/3}\left(\frac{Ek}{Pr}\right)^{1/3}, \tag{3.4}$$

$$\omega_c = (2-3\,Pr^2)^{1/2}\left(\frac{2\pi}{1+Pr}\right)^{2/3}\left(\frac{Ek}{Pr}\right)^{1/3}, \tag{3.5}$$

where ω_c is the oscillation frequency at the onset. Thus the onset length scale ℓ_c in low-Pr convection is larger by a factor of $(1+1/Pr)^{1/3}$.

The flow in the rotating cell for $Ek = 1.45\times10^{-6}$ is shown in figure 3 for various Ra. For this Ek and $Pr = 0.021$, the length scale at the onset of convection according to (3.4) is $\ell_c/H \approx 0.1$, which is equal to the horizontal dimension of the slender domain. Thus the low-Pr flow for this Ek is confined at the onset. For $Ra = 6\times10^7$ – not far from the onset – the Coriolis force dominates the buoyancy force, leading to smooth and tall velocity structures inhabiting the entire depth (figure 3*a*). For $Ra = 2\times10^8$ (figure 3*b*), buoyancy becomes stronger but the flow continues to be influenced by the strong rotation. The observed tall structures develop a wavy character as in high-Pr convection (Cheng *et al.* 2020). The vertical coherence is lost nearly completely for $Ra = 10^9$, and for $Ra = 10^{10}$, the flow morphology appears very close to that in the non-rotating cell shown in figures 2(*f*,*i*), indicating that the effects of the Coriolis force (for this rotation) essentially vanish near $Ra = 10^{10}$. From the velocity streamlines visualization (not shown), we infer that the helical structure, present for the entire range of the thermal forcing explored in the non-rotating cell, is not observed in the rotating slender convection when the Coriolis force dominates; the helical configuration is recovered only when the thermal forcing becomes strong enough to overcome rotation.

Dwindling vertical coherence with increasing Ra, for a fixed rotation, is also clear from the temperature field in figures 3(*e–h*). The temperature isosurfaces for $Ra = 6\times10^7$ – shown in figure 3(*e*) – are nearly flat circular discs. This is in line with the Taylor–Proudman constraint that the vertical variation of the flow is inhibited in a rapidly rotating inviscid flow (Chandrasekhar 1981). With increasing Ra, the isosurfaces become increasingly three-dimensional, and for $Ra = 10^{10}$, appear very similar to the non-rotating case. In § 5, we also show that the integral transport properties of the rotating flow at $Ra = 10^{10}$ and $Ek = 1.45\times10^{-6}$ are nearly the same as those of the corresponding non-rotating flow.

A qualitatively similar change in the flow morphology is observed when the rotation increases for a prescribed thermal forcing (Horn & Shishkina 2015; Aurnou *et al.* 2020). Figure 4 exhibits flow structures for $Ra = 10^{10}$ and $0 \le Ro^{-1} \le 30$, where the helical structure transforms to tall vertically elongated velocity structures as the container is rotated increasingly rapidly. The temperature contours also lose their three-dimensional character as Ro decreases, consistent with the observations in wider convection domains filled with moderate- and high-Pr fluids (Cheng *et al.* 2015). We also observe from figure 4 that the flow length scale varies with varying Ro. For $Ro^{-1} = 30$ in figure 4(*d*), $Ek \approx 4.8\times10^{-8}$ and the linear stability theory yields $\ell_c/H \approx 0.032$, which is nearly three times smaller than that for $Ek \approx 1.45\times10^{-6}$ in figure 3. Therefore, the confinement effects in the slender cell are mitigated progressively as Ek decreases.

4. Rotating slender convection near the onset

We first explore the flow evolution in the low-supercritical regime for $Ek = 1.45\times10^{-6}$ and $Pr = 0.021$. We start simulations from the conduction solution with random

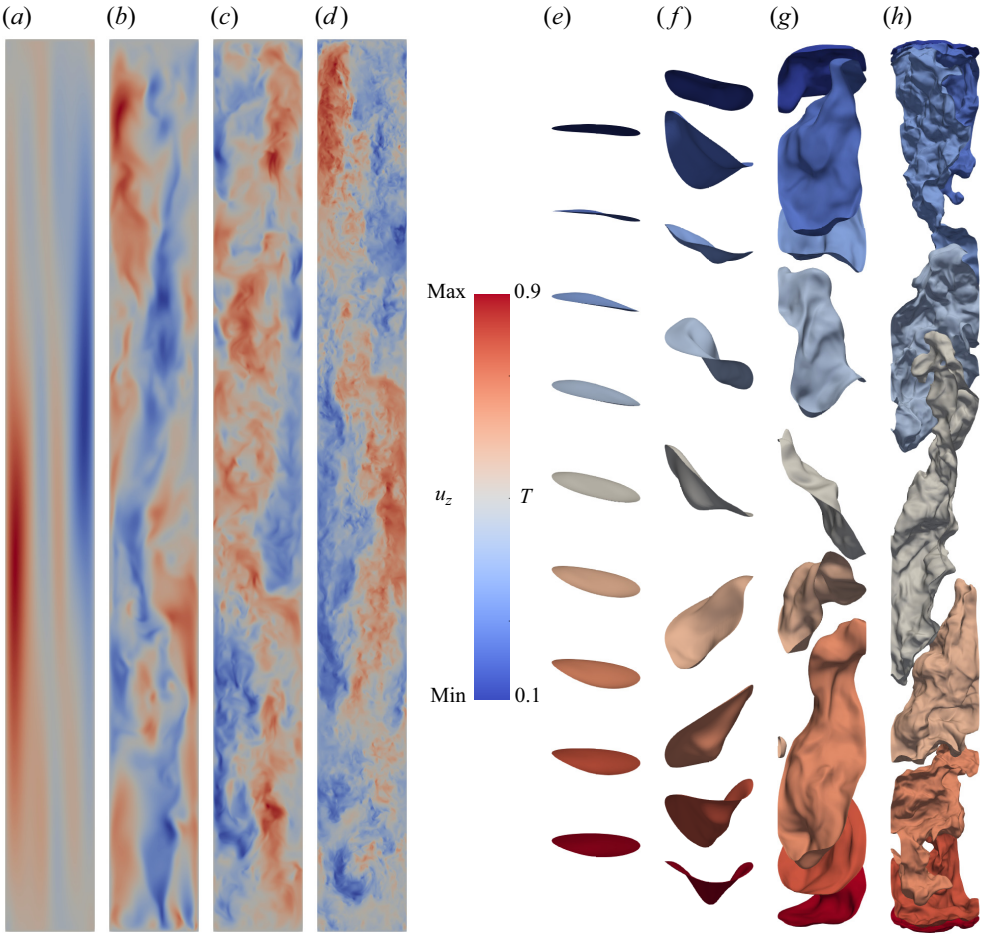

Figure 3. Flow morphology in a rotating slender cell for $Pr = 0.021$, $Ek = 1.45 \times 10^{-6}$, revealed by (*a–d*) instantaneous vertical velocity slices and (*e–h*) temperature isosurfaces, for (*a*,*e*) $Ra = 6 \times 10^7$, (*b*,*f*) $Ra = 2 \times 10^8$, (*c*,*g*) $Ra = 10^9$, and (*d*,*h*) $Ra = 10^{10}$. Near the onset of convection (*a*,*e*), flow structures feel the rotation strongly, and the variation along the vertical direction is almost suppressed. With increasing Ra, the resilience increases and the flow configuration for $Ra = 10^{10}$ (*d*,*h*) shows strong resemblance with its non-rotating counterpart in figure 2. (The global heat and momentum transports are also nearly indifferent for these cases; see table 3.)

perturbations, and observe that the convective state, corresponding to substantially non-zero values of $Nu - 1$, occurs first at $Ra = 5.6 \times 10^7$. Note that this value is nearly an order of magnitude larger than the Ra_c obtained from (3.3). Here, the Nusselt number Nu is computed as

$$Nu = 1 + \sqrt{Ra\,Pr}\,\langle u_z T\rangle_{V,t}, \tag{4.1}$$

where $\langle\cdot\rangle_{V,t}$ denotes averaging over the entire flow and integration time. For a simulation at $Ra = 5.55 \times 10^7$ started from the conduction state, we observe $Nu - 1 \approx 0.0022$, whereas we get $Nu - 1 \approx 0.049$ when the same simulation is started with a flow state given by the simulation at $Ra = 6 \times 10^7$. By decreasing Ra, we can observe finite-amplitude convection up to $Ra = 5.40 \times 10^7$, where the convective flux $Nu - 1 \approx 0.034$ is small but

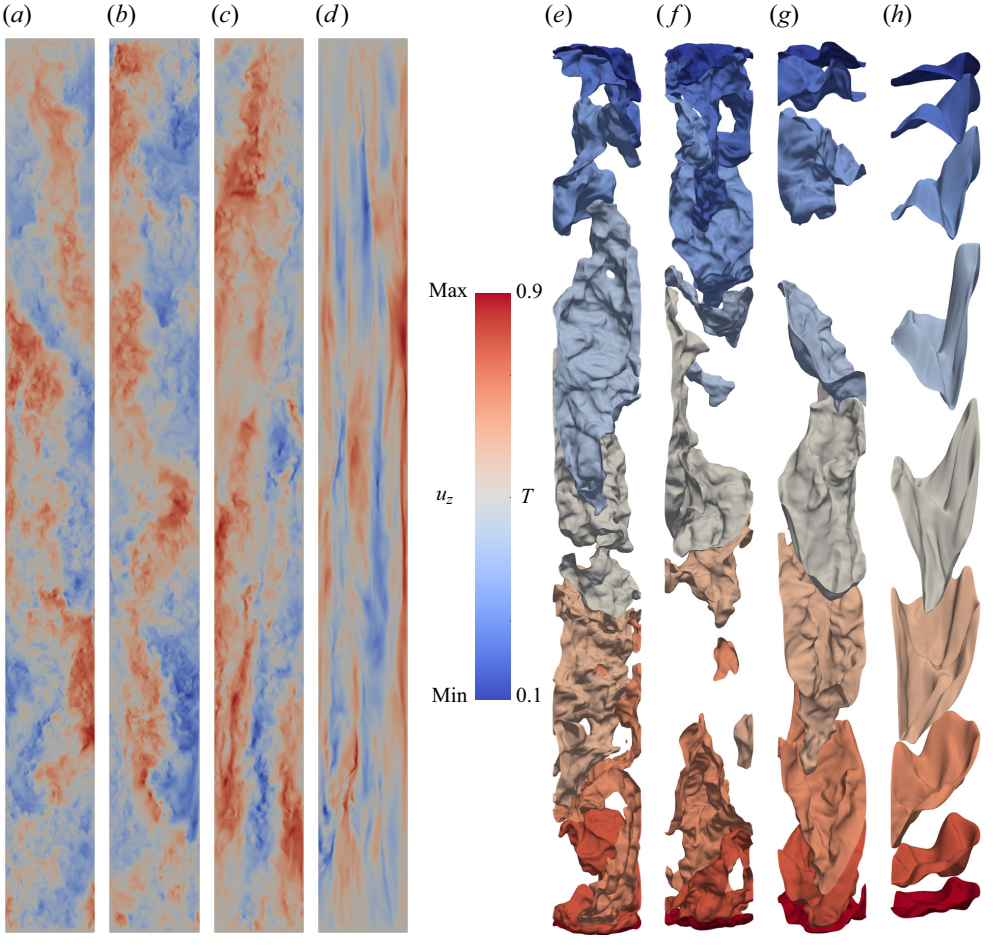

Figure 4. Evolution of the convective structures with increasing rotation rate for $Pr = 0.021$, $Ra = 10^{10}$: (*a*,*e*) $Ro^{-1} = 0$, (*b*,*f*) $Ro^{-1} = 2$, (*c*,*g*) $Ro^{-1} = 10$, (*d*,*h*) $Ro^{-1} = 30$. The flow loses its three-dimensional character, and the length scale of the velocity structures decreases, as the Rossby number decreases.

significantly different from zero. Thus there is modest hysteresis in low-Pr RRBC in a slender cell.

We monitor the evolution of the temperature and velocity fields at a few locations in the flow, and show the temperature variation at mid-height near the sidewall in figure 5 for $Ra \leq 10^8$ and $Ek = 1.45 \times 10^{-6}$. Figure 5(*a*) exhibits that the flow evolves periodically for $Ra = 6 \times 10^7$, a feature also observed for lower-Ra simulations. The corresponding power spectrum, shown in figure 5(*b*), reveals a single dominant frequency at $\omega \approx 0.20$, and its higher harmonics. It is interesting that this frequency agrees well with $\omega_c \approx 0.195$ predicted from (3.5) using the linear stability analysis at $Ek = 1.45 \times 10^{-6}$ (Chandrasekhar 1981). With increasing Ra, the flow evolution becomes progressively complex due to the emergence of other modes. For $Ra = 7 \times 10^7$, a high-amplitude peak develops also at a lower frequency, which indicates the presence of the wall modes (Goldstein *et al.* 1994; Horn & Schmid 2017; Aurnou *et al.* 2018). For $Ra = 8 \times 10^7$, the peak at lower frequency becomes strong compared to its higher-frequency counterpart. The periodicity is nearly lost at $Ra = 9 \times 10^7$, and the flow becomes chaotic. The broadband

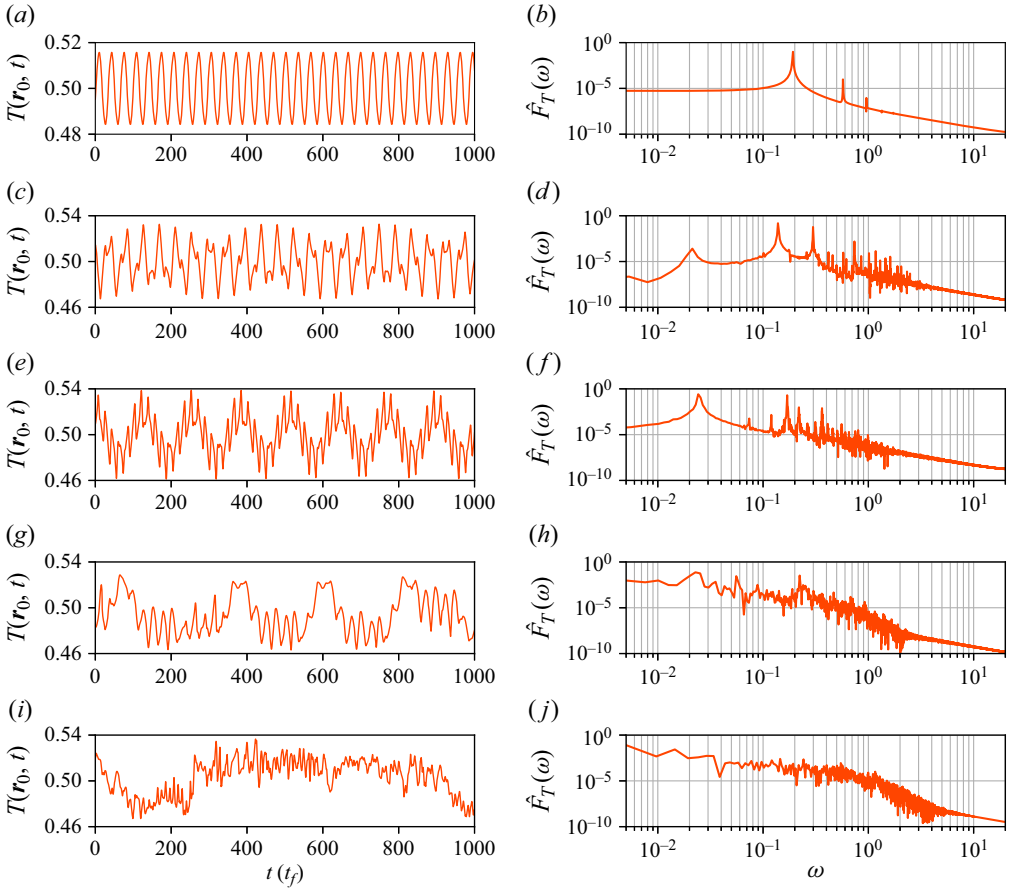

Figure 5. (*a*,*c*,*e*,*g*,*i*) Temperature signal in the mid-plane at a probe near the sidewall, and (*b*,*d*,*f*,*h*,*j*) the corresponding power spectrum in a rapidly rotating flow ($Pr = 0.021$, $Ek = 1.45 \times 10^{-6}$) near the onset of convection: (*a*,*b*) $Ra = 6 \times 10^7$, (*c*,*d*) $Ra = 7 \times 10^7$, (*e*,*f*) $Ra = 8 \times 10^7$, (*g*,*h*) $Ra = 9 \times 10^7$, and (*i*,*j*) $Ra = 10^8$.

power spectrum for $Ra \geq 9 \times 10^7$ indicates the presence of flow structures of a wide range of temporal (and spatial) scales. Thus, due to its highly inertial nature, low-Pr RRBC becomes promptly complex.

Figure 6 shows the instantaneous mid-plane slices of the vertical velocity for $Ra \leq 9 \times 10^7$ in the rotating cell at $Ek = 1.45 \times 10^{-6}$. We can see that the vertical velocity peaks near the sidewall at $Ra = 6 \times 10^7$, while the bulk region (away from the sidewall) is characterized by low-amplitude structures. This is a signature of the wall modes in the slender convection cell at a low Prandtl number (Horn & Schmid 2017; Aurnou *et al.* 2018). For $Ra = 7 \times 10^7$ and 8×10^7, the high-amplitude patch broadens and encroaches into the bulk interior. However, the interior is nearly entirely occupied by the bulk mode at $Ra = 9 \times 10^7$, and has taken over the wall modes (Goldstein *et al.* 1994). Further, the convective flow patterns in rotating cylinders are observed to precess (mostly) in the retrograde direction (Zhong, Ecke & Steinberg 1993; Horn & Schmid 2017). Similar precessing patterns in the slender cell at low Prandtl number can be found

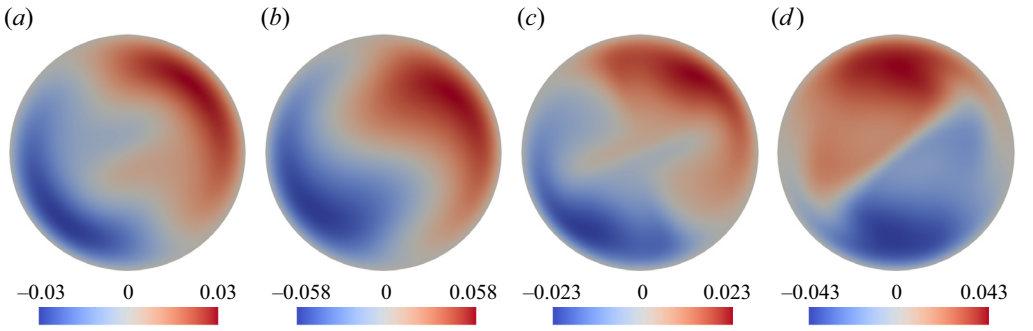

Figure 6. Instantaneous vertical velocity contours in the mid-plane for $Ek = 1.45 \times 10^{-6}$ and (*a*) $Ra = 6 \times 10^7$, (*b*) $Ra = 7 \times 10^7$, (*c*) $Ra = 8 \times 10^7$, (*d*) $Ra = 9 \times 10^7$. Peak amplitudes in the velocity are observed near the sidewall at low Ra, but the interior of the domain is filled with stronger flows as thermal driving becomes stronger.

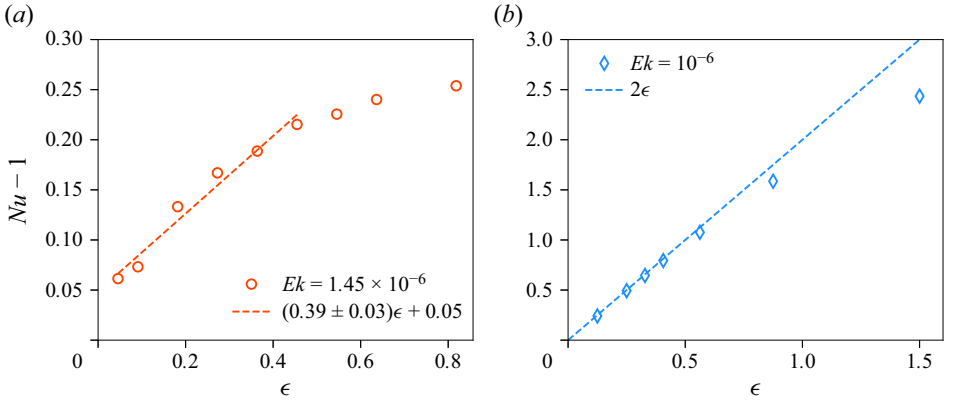

Figure 7. Convective heat transport $Nu - 1$ as a function of the normalized distance $\epsilon = Ra/Ra_c - 1$ from the onset for (*a*) $Pr = 0.021$ and (*b*) $Pr = 1$. Linear scaling is observed in the vicinity of the onset for both cases, but a finite intercept in (*a*) is due to the highly inertial nature of low-Pr convection.

in the supplementary movies for a few cases available at https://doi.org/10.1017/jfm.2024.640.

We now compare the heat transport at the onset in flows at low Pr with those at moderate and high Pr, both rotating. For moderate and high Pr, the convective heat transport $Nu - 1$ has been observed to increase linearly with the supercriticality $\epsilon = Ra/Ra_c - 1$ (Gillet & Jones 2006; Ecke 2015; Gastine, Wicht & Aubert 2016; Long *et al.* 2020; Ecke *et al.* 2022). Figure 7(*a*) shows the present data on $Nu - 1$ as a function of ϵ on a linear–linear scale for $Pr = 0.021$ and $Ek = 1.45 \times 10^{-6}$. Even though there is modest hysteresis (as mentioned earlier), we have taken $Ra_c = 5.5 \times 10^7$ based on the observation that the convective heat transport is very small at $Ra = 5.55 \times 10^7$. Figure 7(*a*) shows a linear trend for $\epsilon \lesssim 0.5$, with the best fit given by $Nu - 1 = 0.39\epsilon + 0.05$. The precise value of the finite intercept depends on the modest hysteresis just mentioned, so is probably not entirely reliable.

The data for unity Prandtl number in the same slender cell at a similar Ekman number, i.e. $Ek = 10^{-6}$, are shown in figure 7(*b*). For this case, the heat transport due to convective motion vanishes at $Ra \approx 8 \times 10^7$, this being the onset Rayleigh number. The data follow the linear scaling quite well; when extrapolated back to $Nu = 1$, one obtains

$Ra_c = 8 \times 10^7$, in perfect agreement with Ra_c determined from inspecting the DNS. It is intriguing that (3.1) yields $Ra_c \approx 8.7 \times 10^8$, which is an order of magnitude higher than the Ra_c determined from DNS data. This is due to wall modes that lower the critical Rayleigh number in confined domains (Herrmann & Busse 1993; Aurnou *et al.* 2018; Vogt *et al.* 2021). Figure 7(*b*) further shows that the prefactor of the linear scaling is ≈ 2, which is close to 1.54 reported recently in a $\Gamma = 1/2$ cell for $Pr = 0.8$ and $Ek = 10^{-6}$ (Ecke 2015; Ecke *et al.* 2022). Thus a slightly different convective heat flux near the onset could be due to the highly inertial nature of low-Pr convection, where the chaotic time dependence is ingrained even at the onset. It appears fair to conclude, overall, that the onset behaviour is essentially the same for all Prandtl numbers.

5. Global transport of heat and momentum in the turbulent state

We now compare the heat transport over an extended range of Ra between rotating and non-rotating cases, both at low $Pr = 0.021$; see figure 8. The data for the non-rotating slender cell (green stars) do not follow a satisfactory power law, but we proceed to fit power laws for different segments of Ra, and comment on them. Let us first note that the critical Rayleigh number for the onset of convection in the slender cell is nearly 1.1×10^7 (Pandey & Sreenivasan 2021), which is much higher than that in unbounded domains (Chandrasekhar 1981). However, the temperature and velocity evolution in the flow as well as the averaged heat flux at the horizontal plates exhibit chaotic time dependence already for $Ra = 2 \times 10^7$. This indicates that the transition to turbulence in the slender cell for $Pr = 0.021$ occurs not far from the onset Ra, which is in line with the observations in wider domains (Schumacher, Götzfried & Scheel 2015; Horn & Schmid 2017). Figure 8 also plots the heat transport from non-rotating convection experiments by Glazier *et al.* (1999) in a $\Gamma = 1/2$ cell, and from DNS by Scheel & Schumacher (2017) in a $\Gamma = 1$ cell, both at $Pr \approx 0.021$. While the heat transport in the slender cell is lower than that reported in wider cells, the discrepancy decreases with increasing Ra; the slender data at the largest Ra explored in this work follow a scaling similar to that in wider convection cells.

It is well known that rotation reduces heat transport (Chandrasekhar 1981; Plumley & Julien 2019; Kunnen 2021; Ecke & Shishkina 2023). The data for $Ek = 1.45 \times 10^{-6}$ (figure 8, red circles) confirm this behaviour – except for large $Ra \geq 10^9$, for which the Nusselt numbers in rotating and non-rotating cases are quite close, and for these particular conditions, Nu can be said to be essentially unaffected by rotation, and the data nearly follow the canonical non-rotating $Ra^{1/3}$ scaling (Niemela *et al.* 2000) – indicating that the effects of rotation on the low-Pr convection in the slender cell resemble those in wider domains.

Turning attention to low Ra for, say, $Ra < 10^8$, Nu is seen to follow a much steeper scaling, $Nu - 1 \sim Ra^3$ (solid red line). (This does not contradict the linear scaling shown in figure 7(*a*), as these plots use different quantities.) This scaling regime is similar to that reported in DNS in a horizontally periodic box for $Pr = 1$ (Song, Shishkina & Zhu 2024). Note that a steep heat transport scaling $Nu \sim Ra^3$ near the onset of rotating convection has been proposed by King *et al.* (2012), thus reported for moderate Prandtl numbers (Stellmach *et al.* 2014; Cheng *et al.* 2015). However, our Nu versus Ra plot (not shown) does not show this cubic scaling near the onset.

In the intermediate region $10^8 < Ra < 10^9$, the data for the rotating case seem to follow a power law with the best fit given by $Nu - 1 \sim Ra^{1.32 \pm 0.06}$. This scaling is roughly consistent with simulations of the asymptotically reduced equations – describing RBC

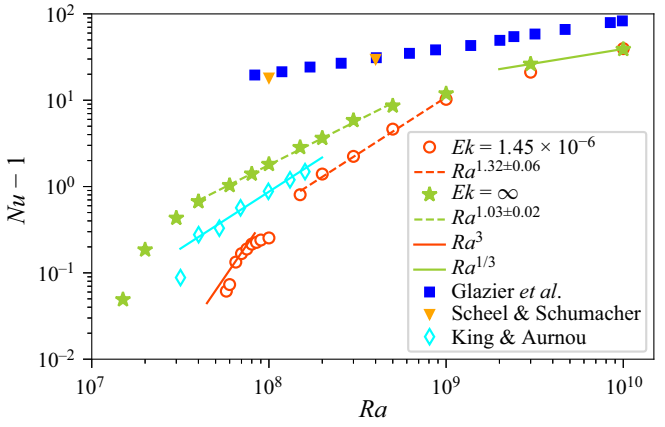

Figure 8. Convective heat transport as a function of Ra in the non-rotating slender cell (green stars) and in a rapidly rotating slender cell (red circles) of $\Gamma = 0.1$ for $Pr = 0.021$. Heat flux in the non-rotating cell exhibits a steeper scaling $Nu - 1 \sim Ra^{1.03}$ (dashed green line) compared to that observed in wider convection cells for moderate Rayleigh numbers, but a similar $Ra^{1/3}$ scaling for large Rayleigh numbers (solid green line). The Nu in rotating convection is lower than in non-rotating convection when Rayleigh numbers are small, but the differences essentially diminish as the thermal forcing increases. The data for $10^8 < Ra \leq 10^9$ exhibit a power law, and the best fit yields $Nu - 1 \sim Ra^{1.32}$ (dashed red line), which is close to $Nu - 1 \sim Ra^{3/2}$ scaling in the geostrophic regime. Cyan diamonds represent experimental data for $Ek = 10^{-6}$ in a $\Gamma = 1$ cylinder from King & Aurnou (2013), and the solid cyan line indicates $Ra^{1.32}$ scaling. Solid lines are not the best fits but are drawn as a guide to the eye. Filled symbols correspond to low-Pr non-rotating convection from the literature: blue squares represent the experimental data from Glazier *et al.* (1999) in the $\Gamma = 1/2$ domain, whereas orange triangles correspond to DNS data in a $\Gamma = 1$ cell by Scheel & Schumacher (2017).

in the rapidly rotating limit – for which $Nu - 1$ increases as $Ra^{3/2}$, for $Pr \geq 0.3$, in the geostrophic regime (Julien *et al.* 2012*a*). A plot of Nu versus Ra (not shown) gives a lower exponent of 0.95 for the same range of Ra, which is similar to $Nu \sim Ra^{0.91}$ observed in the 'rotationally dominated' regime of convection in liquid gallium in a $\Gamma = 1.94$ cylinder (Aurnou *et al.* 2018). Moreover, $Nu - 1 \sim Ra^{1.03}$ for intermediate Rayleigh numbers in the non-rotating case. For comparison, we also include data from King & Aurnou (2013), who performed experiments in a $\Gamma = 1$ cylindrical cell for $Pr \approx 0.025$: cyan diamonds in figure 8 show the heat transport for $Ek = 10^{-6}$. It is clear that $Nu - 1$ in the wider RRBC cell also increases steeply near the onset, but for higher Ra, $Nu - 1$ exhibits a similar $Ra^{1.32}$ scaling (solid cyan line) as observed in the rotating slender cell.

Rotation also influences momentum transport, as seen by the behaviour of the Reynolds number, based here on the root mean square (r.m.s.) velocity and the depth of the fluid layer, as

$$Re = \sqrt{\langle u_x^2 + u_y^2 + u_z^2 \rangle_{V,t}}\, Ra/Pr. \tag{5.1}$$

The Reynolds number in both the non-rotating and rotating cells is plotted as a function of Ra in figure 9. The Re for the non-rotating cell (green stars) increases rapidly near the onset, but the rate of increase decays as the thermal driving becomes stronger. In the same intermediate range of Ra where we observe $Nu - 1 \sim Ra$ scaling, the best fit yields $Re \sim Ra^{0.73\pm0.01}$ scaling. Note that the Reynolds number in wider convection domains has been known to increase nearly as $\sqrt{Ra}$ for moderate and low Prandtl numbers (Ahlers, Grossmann & Lohse 2009; Chillà & Schumacher 2012; Pandey & Verma 2016; Scheel & Schumacher 2017; Verma, Kumar & Pandey 2017; Pandey *et al.* 2022*b*). We indicate the

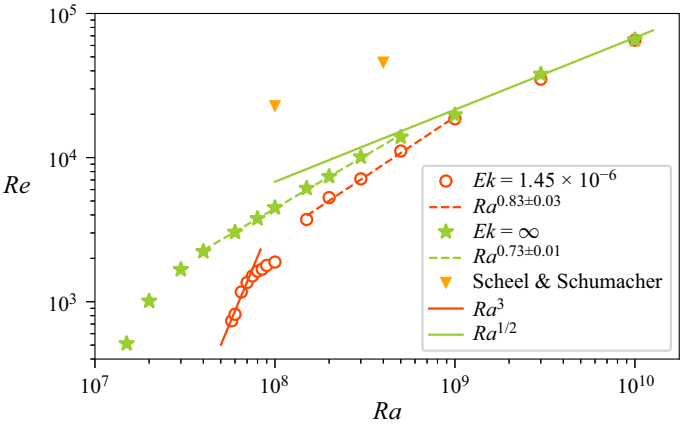

Figure 9. Reynolds number Re as a function of Ra in the non-rotating cell (green stars) and rotating cell at $Ek = 1.45 \times 10^{-6}$ (red circles). Velocity fluctuations grow rapidly near the onset of convection in the slender cell, but the growth rate becomes slower as the driving becomes stronger. The solid green line indicates that the data at the highest Ra nearly follow a $\sqrt{Ra}$ power law as in wider cells. The solid red line suggests that Re grows as Ra^3 for $Ra < 10^8$. Dashed lines represent the best fits for moderate thermal forcings. The difference between the non-rotating and rotating Re values declines as Ra increases, and the two are nearly indistinguishable at $Ra = 10^{10}$. Orange triangles represent DNS data in a $\Gamma = 1$ cell by Scheel & Schumacher (2017).

$Ra^{1/2}$ scaling by a solid green line in figure 9, and note that the non-rotating data for the largest few Rayleigh numbers of this study nearly follow this same scaling, signalling that the effects of confinement become weaker with increasing thermal driving. Also included in figure 9 for comparison are Re computed in a $\Gamma = 1$ cylindrical cell for $Pr = 0.021$ by Scheel & Schumacher (2017). We observe that the Reynolds number in the slender cell is smaller compared to that in the wider cell, which is due to a larger effective friction of rigid boundaries in the former case (Pandey & Sreenivasan 2021).

Red circles in figure 9 represent the Reynolds numbers in the rotating slender cell for $Ek = 1.45 \times 10^{-6}$, and the reduced transport of momentum in the presence of rotation is clear (Schmitz & Tilgner 2010) for low Ra. The figure also shows, similar to figure 8, that the onset of convection shifts to higher Ra compared to that for the non-rotating cell. Near the convective onset, Re in the rotating cell grows approximately as Ra^3 (solid red line), very similar to the growth of $Nu - 1$ in this regime. A rapid growth of Re near the onset of rotating convection was also reported by Schmitz & Tilgner (2010), who performed DNS in a horizontally periodic domain. With increase of the thermal driving, the growth rate of Re decays, and the best fit for $10^8 < Ra \leq 10^9$ is a $Re \sim Ra^{0.83\pm0.03}$ scaling (dashed red line). This scaling has some similarity with the dissipation-free scaling $Re \sim Ra\,Ek/Pr$ reported by Guervilly, Cardin & Schaeffer (2019), Maffei *et al.* (2021), Vogt *et al.* (2021) and Ecke & Shishkina (2023). For higher Ra, Re in the rotating cell approaches that in the non-rotating cell, and the difference becomes very small for $Ra > 10^9$.

The influence of rotation can be studied also by decreasing the Rossby number Ro for a fixed Rayleigh number (Kunnen *et al.* 2011; Stevens, Clercx & Lohse 2013; Ecke & Niemela 2014; Horn & Shishkina 2015; Aurnou *et al.* 2020); the inverse Rossby number Ro^{-1} is a measure of the strength of the Coriolis force relative to buoyancy. We carry out low-Pr simulations for $Ro^{-1} \in [0, 30]$ at $Ra = 10^8, 10^9, 10^{10}$. The Nusselt number normalized with Nu_0 – the heat transport in absence of rotation – as a function of Ro^{-1} is shown in figure 10(*a*), with the curves for different Ra collapsing reasonably well. The normalized heat flux remains close to unity for $Ro^{-1} \lesssim 2$, beyond which it decreases.

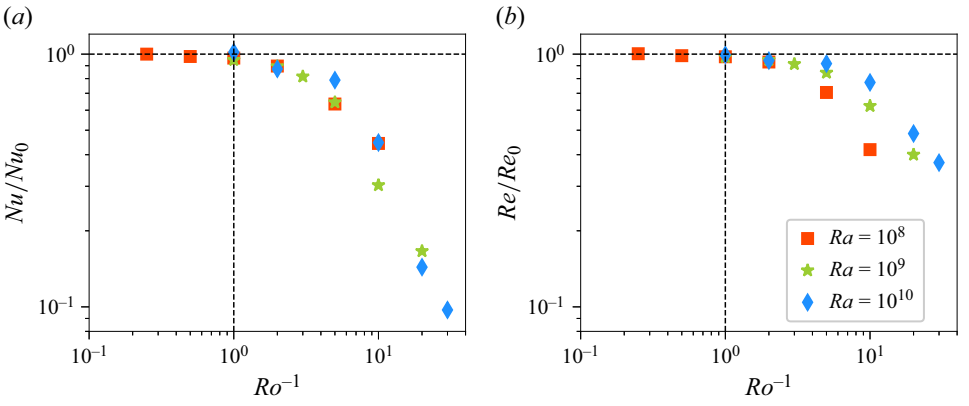

Figure 10. (*a*) Heat and (*b*) momentum transports in rotating slender cells, normalized with the corresponding values from the non-rotating cell, are nearly unity for $Ro^{-1} \leq 2$, but decay rapidly for larger inverse Rossby numbers. The suppression of the heat flux is stronger than that of the momentum flux in low-Pr slender convection.

This indicates that slow rotation does not affect the heat transport in the slender cell, in line with observations in wider convection cells for moderate Prandtl numbers (Wedi *et al.* 2021). Figure 10 also shows that there is no enhancement of heat transport at moderate rotation rates, in contrast to that at large Prandtl numbers due to the so-called 'Ekman pumping' mechanism (Stevens *et al.* 2009; Zhong *et al.* 2009; Zhong & Ahlers 2010; Chong *et al.* 2017), but the absence of heat flux enhancement in the slender cell data is consistent with low-Pr RRBC in more extended domains (Zhong *et al.* 2009).

The normalized Reynolds number Re/Re_0 with Ro^{-1} is plotted in figure 10(*b*). The trend is qualitatively similar to that of the normalized heat flux; weak rotation ($Ro^{-1} \lesssim 2$) does not affect momentum transport. For $Ro^{-1} \gtrsim 2$, the normalized momentum flux decreases, but the data for $Ra = 10^8$ lie below those for $Ra \geq 10^9$ at higher Ro^{-1}. The suppression of the momentum transport is weaker than for heat transport; at $Ro^{-1} = 10$, the normalized Nusselt number is $Nu/Nu_0 \approx 0.45$, whereas $Re/Re_0 \approx 0.8$, both for $Ra = 10^{10}$.

6. Temperature gradient in the bulk region and viscous boundary layer

The mean temperature in turbulent convection varies primarily in the thin thermal boundary layers near the horizontal plates. However, severe lateral confinement causes temperature variation to be present also in the bulk region for moderate and low Prandtl numbers (Iyer *et al.* 2020; Pandey & Sreenivasan 2021; Pandey *et al.* 2022*a*). The mean vertical temperature gradient $\partial T/\partial z$ decreases with increasing Ra in the non-rotating case, whereas it changes in a specific manner in rotating convection (Julien *et al.* 2012*b*; Cheng *et al.* 2020; Aguirre Guzmán *et al.* 2022). We compute mean vertical temperature gradient in the bulk region, $\langle \partial T/\partial z \rangle_{\text{bulk}}$, by performing an average over the bulk volume with $z/H \in [0.25, 0.75]$, and plot it as a function of Ra in figure 11(*a*) for $Pr = 0.021$. The gradient remains close to unity and does not change significantly near the onset of non-rotating convection (green stars). Thus the bulk flow state in the vicinity of the onset does not differ much from the unmixed conduction state with $\partial T/\partial z = -1$. For $Ra > 10^8$, however, $-\langle \partial T/\partial z \rangle_{bulk}$ decreases monotonically with Ra, but even for $Ra = 10^{10}$, low-Pr RBC in the slender cell possesses a higher gradient than in the well-mixed case of extended domains.

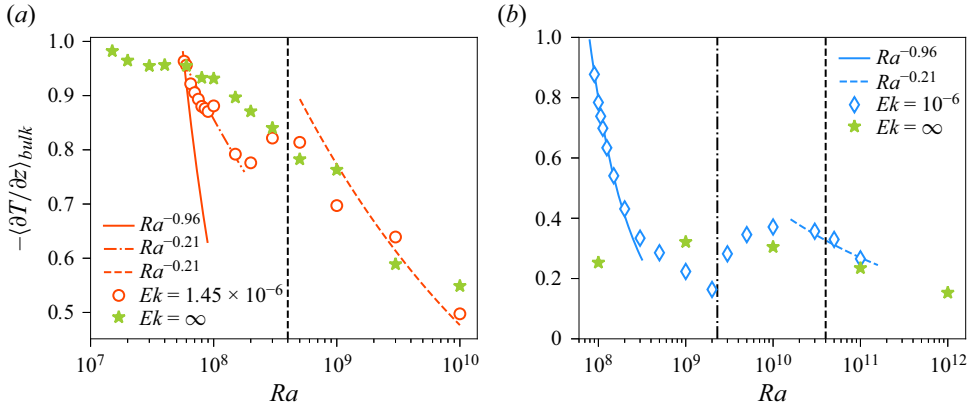

Figure 11. Mean vertical temperature gradient in the bulk region between $z = 0.25H$ and $z = 0.75H$ as a function of Ra from non-rotating (green stars) and rotating (open symbols) slender cells for (*a*) $Pr = 0.021$ and (*b*) $Pr = 1$. Mean gradient decreases monotonically with Ra in the non-rotating convection, whereas a non-monotonic trend is observed in the rotating convection. Solid and dashed curves are guides to the eye and not the best fits. The dash-dotted vertical line in (*b*) indicates the transition $Ra \approx 23\,Ek^{-4/3}$ between the cellular and plumes regimes, as found by Stellmach *et al.* (2014). Dashed vertical lines in both plots correspond to $Ro = 0.2$. Non-rotating data in (*b*) are taken from Iyer *et al.* (2020).

The variation of $\langle \partial T/\partial z \rangle_{bulk}$ in figure 11(*a*) for rotating convection (red circles) is different. It has been known from simulations of the asymptotically reduced equations (Sprague *et al.* 2006; Julien *et al.* 2012*b*) as well as DNS of RRBC (Stellmach *et al.* 2014; Aguirre Guzmán *et al.* 2022) that the temperature gradient decreases steeply with Ra in the cellular and columnar regimes, which occur in the vicinity of convective onset for moderate and large Prandtl numbers. With further increase of Ra, the gradient increases in the plumes regime and nearly saturates in the geostrophic regime, where the vertical coherence is lost (Stellmach *et al.* 2014). For higher Rayleigh numbers in the rotation-affected regime, the gradient decreases again (Cheng *et al.* 2020). Figure 11(*a*) shows that the gradient for $Ek = 1.45 \times 10^{-6}$ decreases rapidly near the onset and starts to increase at $Ra = 2 \times 10^8$, before decreasing again for $Ra \geq 5 \times 10^8$.

Figure 11(*b*) shows the temperature gradient for $Pr = 1$ from the rotating case ($Ek = 10^{-6}$) and the non-rotating case (data taken from Iyer *et al.* 2020), both for slender cells. The bulk temperature gradient varies with Ra qualitatively the same way as in the low-Pr rotating convection. Near the critical Rayleigh number, the gradient follows an $Ra^{-0.96}$ scaling indicated by the solid blue curve. This scaling is consistent with the onset results in simulations of asymptotic equations (Sprague *et al.* 2006; Julien *et al.* 2012*b*) as well as with the DNS (King *et al.* 2013; Stellmach *et al.* 2014; Aguirre Guzmán *et al.* 2022) for moderate Prandtl numbers. With increasing Ra, the gradient decreases more slowly before increasing from $Ra = 2 \times 10^9$ up to $Ra \approx 6 \times 10^9$. As discussed earlier, an increasing gradient with Ra is a characteristic of the plumes region. Stellmach *et al.* (2014) performed DNS in a horizontally periodic domain with both no-slip and free-slip plates, and observed that the transition for $Pr = 1$ from the cellular to plumes region occurs at $Ra \approx 23\,Ek^{-4/3}$ for the no-slip case. This corresponds to $Ra \approx 2.3 \times 10^9$ for the slender data; we indicate this transition Ra by the dash-dotted vertical line in figure 11(*b*). It is interesting that the transition Ra found for a horizontally periodic domain identifies the transition for the slender data quite well. It is observed in experiments (Cheng *et al.* 2020) and DNS

(Aguirre Guzmán *et al.* 2022) that the temperature gradient decreases as $Ra^{-0.21}$ in the rotationally affected regime, when the thermal forcing is significantly stronger than the critical value for the onset. The slender data at the largest Rayleigh numbers in figure 11(*b*) nearly follow this scaling. Thus the temperature gradient with Ra in the rotating slender cell is qualitatively similar to that in wider cells, indicating again the dominance of rotation over confinement.

To see if the data in figure 11(*a*) exhibit the scaling features just mentioned for moderate Prandtl numbers, we indicate the $Ra^{-0.96}$ scaling by a solid red curve, but find that the gradient near the onset decreases more slowly; instead, the data follow a $\langle \partial T/\partial z \rangle_{bulk} \sim Ra^{-0.21}$ scaling (red dash-dotted curve). This is possibly an indication of a different flow state near the onset in low-Pr convection. The $Ra^{-0.21}$ scaling in the rotation-affected regime is also indicated as a red dashed curve; we find from this exercise that the gradient for the largest Ra in the low-Pr case is not very different. The dashed vertical lines in figure 11 correspond to $Ro = 0.2$, which suggests that the $Ra^{-0.21}$ scaling occurs when $Ro > 0.2$ and the rotational constraint in bulk region relaxes gradually.

The thickness of the viscous boundary layer (VBL) near the horizontal plates decreases with increasing Ra in non-rotating convection (King *et al.* 2013; Scheel & Schumacher 2017; Bhattacharya *et al.* 2018). In rotating convection, however, the VBL – also known as the Ekman layer – is controlled by the Ekman number; for weak thermal forcings, i.e. in a rotationally controlled regime, the Ekman layer thickness scales as $\sqrt{Ek}$ (King *et al.* 2013; Aguirre Guzmán *et al.* 2022). The VBL thickness δ_u is frequently determined using the r.m.s. horizontal velocity profile $u_h(z)$, where $u_h = \sqrt{\langle u_x^2 + u_y^2 \rangle_{A,t}}$. Due to the imposed no-slip condition in our simulations, u_h vanishes at the plates and increases rapidly as one moves away from them. We estimate δ_u as the distance of the first local maximum in the $u_h(z)$ profile from the horizontal plate. We compute δ_u at both the top and bottom plates, and show the averaged thickness as a function of Ra in figure 12(*a*) for both the non-rotating and rotating slender cells. For the non-rotating case (green stars), δ_u decreases with Ra. In figure 12(*b*), we plot the same data as a function of Re, which suggests that data for $Re > 10^3$ may be described by a single power law. The best fit for this regime yields a $\delta_u = 0.05\, Re^{-0.26}$ scaling, which is in qualitative agreement with the $Re^{-1/4}$ scaling observed in wider convection domains for moderate and high Prandtl numbers (King *et al.* 2013).

The Ekman layer thickness for $Ek = 1.45 \times 10^{-6}$ in figure 12(*a*) is nearly independent of Ra for $Ra \leq 10^8$. The constancy of δ_u suggests that the VBL in this regime behaves as the classical Ekman layer, which results from the balance between the viscous and Coriolis forces (King *et al.* 2013). Figure 12(*a*) also reveals that a considerable variation in δ_u is observed for higher Rayleigh numbers. Further, the difference between the rotating and non-rotating data becomes very small for $Ra \geq 10^9$, which indicates the increasing dominance of thermal forcing over rotation as Ra increases. To see the Ek dependence of δ_u, we plot the normalized thickness $\delta_u/\sqrt{Ek}$ as a function of Ra in figure 12(*c*), and also include the data from the $Pr = 1$, $Ek = 10^{-6}$ simulations. The figure shows that the $\delta_u \sim \sqrt{Ek}$ scaling is indeed observed for both the Prandtl numbers at low thermal forcings and the prefactor ≈ 3 for $Pr = 0.021$, and ≈ 3.5 for $Pr = 1$ simulations. These prefactors are in the range of values reported in RRBC in wider domains (King *et al.* 2013; Aguirre Guzmán *et al.* 2022). Figure 12(*c*) also shows that the range of Rayleigh numbers over which the VBL is of the Ekman type is wider for $Pr = 1$ than for $Pr = 0.021$, which indicates the inertial nature of low-Pr RRBC and is consistent with the findings of Aguirre Guzmán *et al.* (2022).

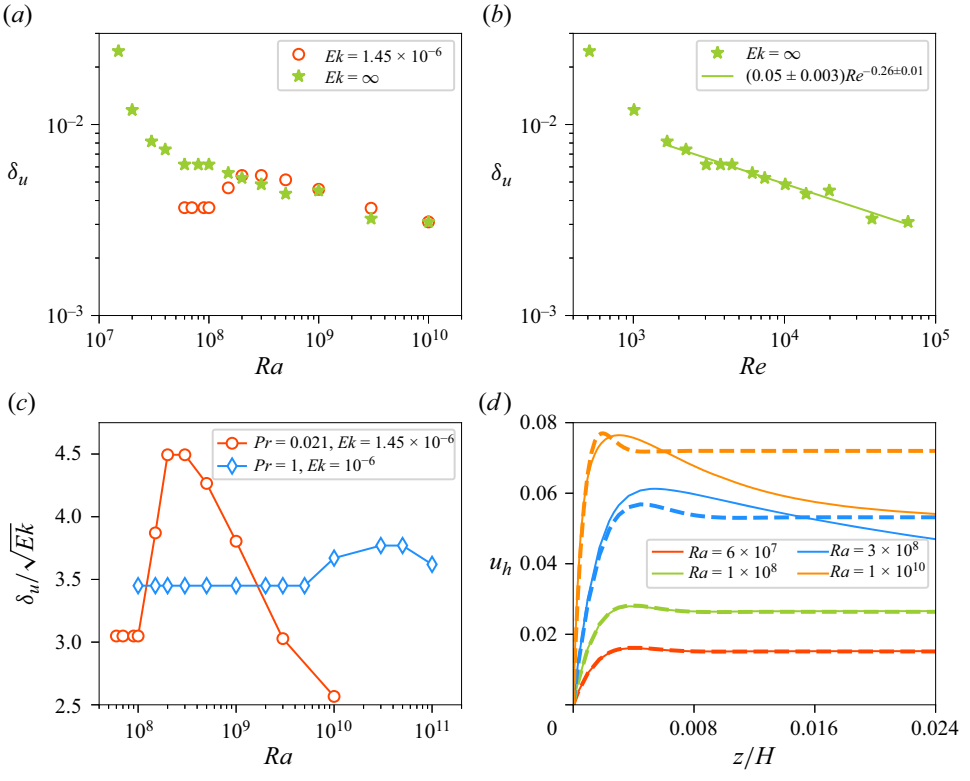

Figure 12. (*a*) Viscous boundary layer thickness for $Pr = 0.021$, averaged over both the horizontal plates, decreases with Ra in the non-rotating slender cell, whereas it remains constant at low Ra in the rotating cell. (*b*) Thickness in the non-rotating cell as a function of Re. The best fit for $Re > 10^3$ shows that $\delta_u \sim Re^{-1/4}$. (*c*) Normalized Ekman layer thickness $\delta_u/\sqrt{Ek}$ remains a constant for a wider range of Ra for $Pr = 1$ than for $Pr = 0.021$ simulations. (*d*) The horizontal velocity profile in the rotating slender cell (solid curves) for $Pr = 0.021$ follows the analytical Ekman layer profile (dashed curves) perfectly up to $Ra = 10^8$, but deviates for larger Rayleigh numbers.

We further probe the Ekman layer in the slender cell by investigating the form of the r.m.s. horizontal velocity profile $u_h(z)$ near the plates. For the classical Ekman layer above a no-slip plate, the velocity profile can be obtained analytically by considering a geostrophic bulk flow, where the horizontal pressure gradients are balanced by the Coriolis forces, and assuming that the same horizontal pressure gradients exist within the boundary layer region. Following Kundu & Cohen (2004) and Aguirre Guzmán *et al.* (2022), we find that $u_h(z)$ near the plate can be described by

$$u_h(z) = U_h[1 - 2\cos(z/\delta_U)\exp(-z/\delta_U) + \exp(-2z/\delta_U)]^{1/2}. \tag{6.1}$$

Here, $U_h = \sqrt{U_x^2 + U_y^2}$ is the r.m.s. horizontal velocity in the geostrophic bulk, with U_x and U_y being the horizontal velocity components. The parameter δ_U corresponds to the thickness of the Ekman layer. In figure 12(*d*), we show $u_h(z)$ for four Rayleigh numbers from the simulations at $Pr = 0.021$, $Ek = 1.45 \times 10^{-6}$ as solid curves. We fit these profiles using (6.1), and determine the parameters U_h and δ_U, and the resulting profiles obtained from (6.1) with the fitted parameters are exhibited as dashed curves in figure 12(*d*). We observe that the profiles for $Ra \leq 10^8$ can be described excellently by the analytical profile (6.1). However, deviation starts to appear for $Ra \geq 1.5 \times 10^8$.

Figure 12(*d*) exhibits that (6.1) still describes the near-wall profiles for all Rayleigh numbers. Thus the VBL in the slender cell for $Pr = 0.021$ is of the Ekman type only up to $Ra = 10^8$, which is consistent with the inference from figure 12(*c*). Note that similar results were reported in RRBC in horizontally periodic boxes by Aguirre Guzmán *et al.* (2022).

7. Conclusions

The centre of attention in this paper is convection of low-Pr fluids (chosen here to be 0.021) at a range of Rayleigh numbers up to 10^{10}, with variable rotation rates. For comparison, we have also performed simulations for $Pr = 1$. By necessity, the aspect ratio is small. From a comparison of the present results with those for several different conditions, including convection in wider cells (where possible), we deduce a variety of results, a few of which are listed below.

First, the flow structure, which is initially helical, develops progressively finer components with increasing thermal forcing. The flow structure feels the rotation strongly near the onset, with suppressed variation along the vertical direction. With increasing Ra, however, the resilience increases and the flow configuration for $Ra = 10^{10}$ (figures 3*d*,*h*) shows a strong resemblance to its non-rotating counterpart in figure 2. In spite of this feature, the essentially isothermal bulk region, observed to exist in wider convection domains, is absent in the slender cell. Yet the heat transport scaling is the same as in wider cells for a given high Rayleigh number, which shows the secondary role of the bulk flow for global heat transport.

We found that near the onset, the supercritical behaviour is qualitatively independent of Pr. For intermediate Ra, the Nusselt number in the non-rotating slender cell increases steeply with Ra; we found $Nu - 1 \sim Ra$ for $6 \times 10^7 \leq Ra \leq 5 \times 10^8$. This increase is steeper than those in convection domains of $\Gamma \geq 0.5$, where $Nu \sim Ra^\beta$ with $\beta \in [0.25, 0.30]$ have been observed (Cioni, Ciliberto & Sommeria 1997; Glazier *et al.* 1999; Scheel & Schumacher 2017; Schindler *et al.* 2022).

We found that $Nu - 1$ in the rotating cell increases approximately as $Ra^{1.3}$ for the intermediate Rayleigh numbers, which is not very different from the $Nu - 1 \sim Ra^{3/2}$ scaling proposed for the geostrophic regime (Julien *et al.* 2012*a*). Further, we observed a $Nu \sim Ra^{0.95}$ scaling for $10^8 \leq Ra \leq 10^9$, which is close to that found in a wider cell at a similar Prandtl number (Aurnou *et al.* 2018). For $Ra \geq 10^9$, the Nu data agree reasonably well with the canonical $Ra^{1/3}$ scaling observed in non-rotating wider convection cells (Niemela *et al.* 2000). We also studied the effects of increasing rotation on the integral transports and the flow structure for fixed thermal forcings, and observed that these flow properties in the slender cell are altered in a very similar manner to those reported in $\Gamma \geq 0.5$ rotating flows.

We obtained the mean temperature gradient in the bulk region of the rotating slender cells for $Pr = 0.021$ and $Pr = 1$, and found that its variation with Ra is similar to that reported in extended domains. We also analysed the width of the Ekman layer and the velocity profile in the region near the plate, and observed that they exhibit very similar behaviour observed in rapidly rotating convective flows in wider domains. Thus the effects of rotation on the slender convection are similar to those in extended convection, even though the non-rotating case exhibits differing behaviour, as long as Ra is high enough.

We point out that the maximum value of the convective supercriticality, Ra/Ra_c, explored in the present work for $Ek = 1.45 \times 10^{-6}$, is nearly 200. This value is not very large for the non-rotating convection. In RRBC, however, the flow characteristics

change rapidly as Ra/Ra_c increases from unity, and one observes richer dynamical regimes compared to those in non-rotating convection over a relatively shorter range of Ra/Ra_c. In addition to our own observations, we cite Julien *et al.* (2012*b*), Aguirre Guzmán *et al.* (2022) and Ecke & Shishkina (2023) also for supporting evidence.

Our study, which is based on simulations in a slender cell of fixed aspect ratio 0.1, suggests that rotation influences convection more strongly than the geometric confinement. This is an important conclusion, as the rotating convective flows could be explored at higher Rayleigh numbers using slender domains, opening new parameter ranges not accessible to wider convection cells. We reiterate that while with decreasing Γ the sidewall boundary layer is expected to have an increasingly stronger influence on the dynamics of RRBC, the rotation effects often overwhelm other factors. It is, of course, obvious that further studies with varying Γ would help us to better understand the interplay between the effects of rotation and confinement.

Supplementary movies. Supplementary movies are available at https://doi.org/10.1017/jfm.2024.640.

Acknowledgements. We thank J. Schumacher for useful input on the work. We also acknowledge valuable discussions with R. Samtaney, who sadly passed away while the work was in progress. The authors gratefully acknowledge SHAHEEN II of KAUST, Saudi Arabia (under project nos k1491 and k1624) and DALMA and JUBAIL clusters at NYU Abu Dhabi for providing computational resources.

Funding. This material is based upon work supported by Tamkeen under the NYU Abu Dhabi Research Institute grant G1502, and by the KAUST Office of Sponsored Research under Award URF/1/4342-01.

Declaration of interests. The authors report no conflict of interest.

Data availability statement. The data that support the findings of this study are available from the corresponding author upon reasonable request.

Author ORCIDs.
Ambrish Pandey https://orcid.org/0000-0001-8232-6626;
Katepalli R. Sreenivasan https://orcid.org/0000-0002-3943-6827.

Appendix A. Simulation parameters

We collect important parameters of DNS in the non-rotating and rotating slender cells in tables 1 and 2, respectively. Table 3 contains relevant parameters of simulations for fixed Rayleigh numbers and varying rotation rates. In addition to comparing the smallest grid spacing with the Kolmogorov length scale (see § 2), we examine the convergence of the heat flux using different methods (Pandey *et al.* 2022*a*); a properly resolved simulation should yield the same global heat transport when computed from different approaches. The exact relations of RBC link the volume- and time-averaged thermal and kinetic energy dissipation rates with the Nusselt number (Shraiman & Siggia 1990), and the heat fluxes from the energy and the thermal dissipation rates are estimated as

$$Nu_{\varepsilon_u} = 1 + \frac{H^4}{\nu^3}\frac{Pr^2}{Ra}\langle \varepsilon_u \rangle_{V,t}, \tag{A1}$$

$$Nu_{\varepsilon_T} = \frac{H^2}{\kappa(\Delta T)^2}\langle \varepsilon_T \rangle_{V,t}. \tag{A2}$$

Ra	$N_e \times N^3$	Nu	Re	t_{sim} (t_f)	Δ_z/η
1.5×10^7	$192\,000 \times 3^3$	1.05 ± 0.001	512 ± 1	2547	0.32
2×10^7	$192\,000 \times 3^3$	1.19 ± 0.001	1010 ± 1	1448	0.47
3×10^7	$192\,000 \times 3^3$	1.43 ± 0.004	1673 ± 1	1255	0.65
4×10^7	$192\,000 \times 3^3$	1.67 ± 0.07	2230 ± 13	950	0.78
6×10^7	$192\,000 \times 3^3$	2.03 ± 0.07	3037 ± 6	997	0.97
8×10^7	$192\,000 \times 3^3$	2.40 ± 0.01	3775 ± 8	995	1.12
1×10^8	$192\,000 \times 3^3$	2.81 ± 0.001	4496 ± 4	929	1.26
1.5×10^8	$192\,000 \times 5^3$	3.84 ± 0.1	6125 ± 11	269	1.00
2×10^8	$192\,000 \times 5^3$	4.64 ± 0.09	7400 ± 15	385	1.14
3×10^8	$192\,000 \times 7^3$	6.84 ± 0.42	$10\,114 \pm 30$	140	1.04
5×10^8	$192\,000 \times 7^3$	9.60 ± 0.07	$13\,896 \pm 3$	110	1.30
1×10^9	$537\,600 \times 7^3$	12.9 ± 0.63	$19\,800 \pm 55$	61.5	1.24
3×10^9	$537\,600 \times 7^3$	27.2 ± 0.66	$37\,905 \pm 122$	36.9	2.00
1×10^{10}	$537\,600 \times 13^3$	39.9 ± 8.5	$65\,715 \pm 804$	29.2	1.69

Table 1. Parameters of DNS for $Pr = 0.021$ in the non-rotating cylindrical cell of $\Gamma = 0.1$: the number of mesh cells $N_e \times N^3$ in the entire flow domain, where N_e is the number of elements and N is the polynomial order of the Lagrangian interpolation; Nu is the globally averaged heat transport estimated using (4.1), and Re is the Reynolds number based on the r.m.s. velocity. Integration time in free-fall units in the statistically steady state is represented by t_{sim}, and the maximum value of the ratio of the local vertical grid spacing $\Delta_z(z)$ to the local Kolmogorov scale $\eta(z)$ is shown in the last column. Error bars indicate the difference in the mean values of the two halves of the data sets.

Ra	$N_e \times N^3$	Nu	Re	t_{sim} (t_f)	Δ_z/η
5.75×10^7	$192\,000 \times 3^3$	1.061 ± 0.001	737 ± 1	1947	0.47
6.0×10^7	$192\,000 \times 3^3$	1.073 ± 0.001	818 ± 1	1890	0.50
6.5×10^7	$192\,000 \times 3^3$	1.133 ± 0.002	1167 ± 1	1434	0.59
7.0×10^7	$192\,000 \times 3^3$	1.167 ± 0.001	1360 ± 1	2301	0.63
7.5×10^7	$192\,000 \times 3^3$	1.189 ± 0.005	1510 ± 1	2579	0.69
8.0×10^7	$192\,000 \times 3^3$	1.215 ± 0.001	1629 ± 1	2475	0.72
8.5×10^7	$192\,000 \times 3^3$	1.226 ± 0.003	1684 ± 1	2423	0.73
9.0×10^7	$192\,000 \times 3^3$	1.240 ± 0.007	1786 ± 1	2390	0.74
1.0×10^8	$192\,000 \times 3^3$	1.254 ± 0.012	1885 ± 4	1288	0.77
1.5×10^8	$192\,000 \times 3^3$	1.80 ± 0.03	3719 ± 9	454	1.13
2×10^8	$192\,000 \times 3^3$	2.39 ± 0.02	5276 ± 9	355	1.42
3×10^8	$192\,000 \times 5^3$	3.24 ± 0.07	7121 ± 20	190	1.11
5×10^8	$192\,000 \times 7^3$	5.62 ± 0.32	$11\,109 \pm 51$	125	1.11
1×10^9	$537\,600 \times 7^3$	11.2 ± 0.32	$18\,595 \pm 81$	63.0	1.20
3×10^9	$537\,600 \times 7^3$	22.1 ± 2.8	$34\,989 \pm 330$	54.2	1.90
1×10^{10}	$537\,600 \times 13^3$	40.6 ± 9.0	$65\,306 \pm 742$	30.6	1.66

Table 2. The same DNS parameters as in table 1 for $Pr = 0.021$ in a rapidly rotating cylindrical cell of $\Gamma = 0.1$ for $Ek = 1.45 \times 10^{-6}$.

At the horizontal plates, the heat is entirely transported due to molecular diffusion, and the area-averaged flux at the plates is estimated using the vertical temperature gradient as

$$Nu_{\partial_z T} = -\frac{H}{\Delta T}\left\langle \left(\frac{\partial T}{\partial z}\right)_{z=0,H} \right\rangle_{A,t}. \tag{A3}$$

Ra	Ro^{-1}	$N_e \times N^3$	Nu	Re	t_{sim} (t_f)	Δ_z/η
10^8	0	$192\,000 \times 3^3$	2.81 ± 0.001	4496 ± 4	929	1.26
10^8	0.25	$192\,000 \times 3^3$	2.82 ± 0.13	4515 ± 17	583	1.27
10^8	0.50	$192\,000 \times 3^3$	2.76 ± 0.02	4435 ± 1	583	1.25
10^8	1	$192\,000 \times 3^3$	2.72 ± 0.17	4391 ± 16	583	1.25
10^8	2	$192\,000 \times 3^3$	2.53 ± 0.02	4187 ± 10	706	1.21
10^8	5	$192\,000 \times 3^3$	1.79 ± 0.08	3172 ± 8	723	1.02
10^8	10	$192\,000 \times 3^3$	1.25 ± 0.01	1885 ± 4	1288	0.77
10^9	0	$537\,600 \times 7^3$	12.9 ± 0.72	$19\,823 \pm 60$	61.8	1.24
10^9	1	$537\,600 \times 7^3$	12.3 ± 0.29	$19\,310 \pm 3$	39.7	1.23
10^9	2	$537\,600 \times 7^3$	11.6 ± 0.12	$18\,800 \pm 16$	45.3	1.21
10^9	3	$537\,600 \times 7^3$	10.5 ± 0.84	$18\,104 \pm 206$	45.0	1.18
10^9	5	$537\,600 \times 5^3$	8.34 ± 1.2	$16\,734 \pm 146$	90.8	1.50
10^9	10	$537\,600 \times 5^3$	3.92 ± 0.43	$12\,359 \pm 78$	125	1.20
10^9	20	$537\,600 \times 5^3$	2.15 ± 0.08	7928 ± 40	136	0.95
10^{10}	0	$537\,600 \times 13^3$	39.9 ± 8.5	$65\,715 \pm 804$	29.2	1.69
10^{10}	1	$537\,600 \times 13^3$	40.6 ± 9.0	$65\,306 \pm 742$	30.6	1.66
10^{10}	2	$537\,600 \times 13^3$	34.8 ± 2.3	$61\,958 \pm 202$	24.2	1.62
10^{10}	5	$537\,600 \times 13^3$	31.5 ± 5.2	$60\,277 \pm 1114$	27.9	1.61
10^{10}	10	$537\,600 \times 11^3$	17.8 ± 4.8	$50\,783 \pm 595$	26.8	1.61
10^{10}	20	$537\,600 \times 9^3$	5.73 ± 1.5	$31\,880 \pm 484$	88.4	1.33
10^{10}	30	$537\,600 \times 7^3$	3.88 ± 0.30	$24\,455 \pm 58$	303	1.59

Table 3. Parameters of DNS for $Pr = 0.021$ with varying rotation frequency.

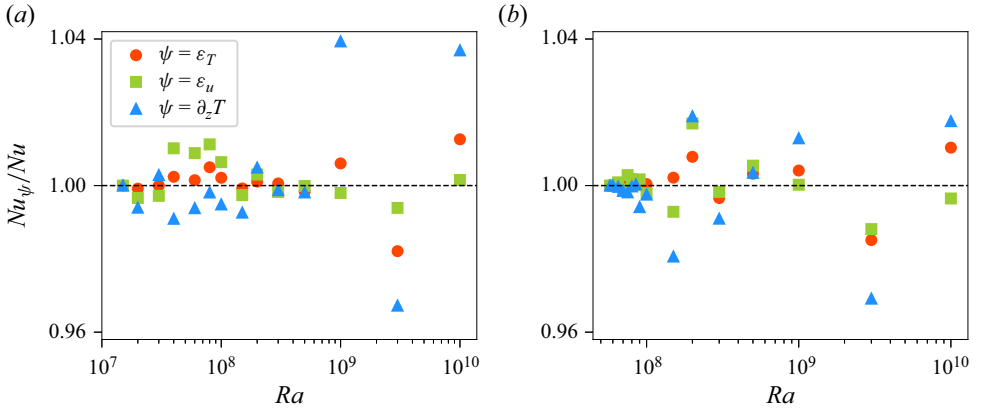

Figure 13. Nusselt numbers computed using the thermal and viscous dissipation rates and the wall temperature gradient agree with Nu computed from (4.1) within 4 % for all simulations. (*a*) The ratios Nu_{ε_T}/Nu, Nu_{ε_u}/Nu and $Nu_{\partial_z T}/Nu$ for $Pr = 0.021$ and $Ek = \infty$. (*b*) Data from the rotating cell for $Ek = 1.45 \times 10^{-6}$.

We plot the ratios Nu_{ε_T}/Nu, Nu_{ε_u}/Nu and $Nu_{\partial_z T}/Nu$ in figure 13(*a*) for the non-rotating simulations, and in figure 13(*b*) for simulations at $Ek = 1.45 \times 10^{-6}$. The ratios depart from unity by a maximum of 4 % for all the simulations, affirming that the simulations are resolved adequately.

References

Aguirre Guzmán, A.J., Madonia, M., Cheng, J.S., Ostilla-Mónico, R., Clercx, H.J.H. & Kunnen, R.P.J. 2022 Flow- and temperature-based statistics characterizing the regimes in rapidly rotating turbulent convection in simulations employing no-slip boundary conditions. *Phys. Rev. Fluids* **7**, 013501.

Ahlers, G., *et al.* 2022 Aspect ratio dependence of heat transfer in a cylindrical Rayleigh–Bénard cell. *Phys. Rev. Lett.* **128**, 084501.

Ahlers, G., Grossmann, S. & Lohse, D. 2009 Heat transfer and large scale dynamics in turbulent Rayleigh–Bénard convection. *Rev. Mod. Phys.* **81**, 503–537.

Aurnou, J., Calkins, M., Cheng, J., Julien, K., King, E., Nieves, D., Soderlund, K. & Stellmach, S. 2015 Rotating convective turbulence in Earth and planetary cores. *Phys. Earth Planet. Inter.* **246**, 52–71.

Aurnou, J.M., Bertin, V., Grannan, A.M., Horn, S. & Vogt, T. 2018 Rotating thermal convection in liquid gallium: multi-modal flow, absent steady columns. *J. Fluid Mech.* **846**, 846–876.

Aurnou, J.M., Horn, S. & Julien, K. 2020 Connections between nonrotating, slowly rotating, and rapidly rotating turbulent convection transport scalings. *Phys. Rev. Res.* **2**, 043115.

Bhattacharya, S., Pandey, A., Kumar, A. & Verma, M.K. 2018 Complexity of viscous dissipation in turbulent thermal convection. *Phys. Fluids* **30** (3), 031702.

Chandrasekhar, S. 1981 *Hydrodynamic and Hydromagnetic Stability*. Dover.

Cheng, J.S., Aurnou, J.M., Julien, K. & Kunnen, R.P.J. 2018 A heuristic framework for next-generation models of geostrophic convective turbulence. *Geophys. Astrophys. Fluid Dyn.* **112** (4), 277–300.

Cheng, J.S., Madonia, M., Aguirre Guzmán, A.J. & Kunnen, R.P.J. 2020 Laboratory exploration of heat transfer regimes in rapidly rotating turbulent convection. *Phys. Rev. Fluids* **5**, 113501.

Cheng, J.S., Stellmach, S., Ribeiro, A., Grannan, A., King, E.M. & Aurnou, J.M. 2015 Laboratory-numerical models of rapidly rotating convection in planetary cores. *Geophys. J. Intl* **201** (1), 1–17.

Chillà, F. & Schumacher, J. 2012 New perspectives in turbulent Rayleigh–Bénard convection. *Eur. Phys. J.* E **35**, 58.

Chong, K.L., Huang, S.-D., Kaczorowski, M. & Xia, K.-Q. 2015 Condensation of coherent structures in turbulent flows. *Phys. Rev. Lett.* **115**, 264503.

Chong, K.L. & Xia, K.-Q. 2016 Exploring the severely confined regime in Rayleigh–Bénard convection. *J. Fluid Mech.* **805**, R4.

Chong, K.L., Yang, Y., Huang, S.-D., Zhong, J.-Q., Stevens, R.J.A.M., Verzicco, R., Lohse, D. & Xia, K.-Q. 2017 Confined Rayleigh–Bénard, rotating Rayleigh–Bénard, and double diffusive convection: a unifying view on turbulent transport enhancement through coherent structure manipulation. *Phys. Rev. Lett.* **119**, 064501.

Cioni, S., Ciliberto, S. & Sommeria, J. 1997 Strongly turbulent Rayleigh–Bénard convection in mercury: comparison with results at moderate Prandtl number. *J. Fluid Mech.* **335**, 111–140.

Ecke, R.E. 2015 Scaling of heat transport near onset in rapidly rotating convection. *Phys. Lett.* A **379** (37), 2221–2223.

Ecke, R.E. & Niemela, J.J. 2014 Heat transport in the geostrophic regime of rotating Rayleigh–Bénard convection. *Phys. Rev. Lett.* **113**, 114301.

Ecke, R.E. & Shishkina, O. 2023 Turbulent rotating Rayleigh–Bénard convection. *Annu. Rev. Fluid Mech.* **55** (1), 603–638.

Ecke, R.E., Zhang, X. & Shishkina, O. 2022 Connecting wall modes and boundary zonal flows in rotating Rayleigh–Bénard convection. *Phys. Rev. Fluids* **7**, L011501.

Favier, B. & Knobloch, E. 2020 Robust wall states in rapidly rotating Rayleigh–Bénard convection. *J. Fluid Mech.* **895**, R1.

Fischer, P.F. 1997 An overlapping Schwarz method for spectral element solution of the incompressible Navier–Stokes equations. *J. Comput. Phys.* **133** (1), 84–101.

Gastine, T., Wicht, J. & Aubert, J. 2016 Scaling regimes in spherical shell rotating convection. *J. Fluid Mech.* **808**, 690–732.

Gillet, N. & Jones, C.A. 2006 The quasi-geostrophic model for rapidly rotating spherical convection outside the tangent cylinder. *J. Fluid Mech.* **554**, 343–369.

Glazier, J., Segawa, T., Naert, A. & Sano, M. 1999 Evidence against 'ultrahard' thermal turbulence at very high Rayleigh numbers. *Nature* **398**, 307–310.

Goldstein, H.F., Knobloch, E., Mercader, I. & Net, M. 1994 Convection in a rotating cylinder. Part 2. Linear theory for low Prandtl numbers. *J. Fluid Mech.* **262**, 293–324.

GUERVILLY, C., CARDIN, P. & SCHAEFFER, N. 2019 Turbulent convective length scale in planetary cores. *Nature* **570**, 368–371.

HANASOGE, S., GIZON, L. & SREENIVASAN, K.R. 2016 Seismic sounding of convection in the Sun. *Annu. Rev. Fluid Mech.* **48**, 191–217.

HEIMPEL, M., AURNOU, J. & WICHT, J. 2005 Simulation of equatorial and high-latitude jets on Jupiter in a deep convection model. *Nature* **438**, 193–196.

HERRMANN, J. & BUSSE, F.H. 1993 Asymptotic theory of wall-attached convection in a rotating fluid layer. *J. Fluid Mech.* **255**, 183–194.

HORN, S. & SCHMID, P.J. 2017 Prograde, retrograde, and oscillatory modes in rotating Rayleigh–Bénard convection. *J. Fluid Mech.* **831**, 182–211.

HORN, S. & SHISHKINA, O. 2015 Toroidal and poloidal energy in rotating Rayleigh–Bénard convection. *J. Fluid Mech.* **762**, 232–255.

IYER, K.P., SCHEEL, J.D., SCHUMACHER, J. & SREENIVASAN, K.R. 2020 Classical 1/3 scaling of convection holds up to $Ra = 10^{15}$. *Proc. Natl Acad. Sci. USA* **117** (14), 7594–7598.

JULIEN, K., KNOBLOCH, E., RUBIO, A.M. & VASIL, G.M. 2012*a* Heat transport in low-Rossby-number Rayleigh–Bénard convection. *Phys. Rev. Lett.* **109**, 254503.

JULIEN, K., RUBIO, A., GROOMS, I. & KNOBLOCH, E. 2012*b* Statistical and physical balances in low Rossby number Rayleigh–Bénard convection. *Geophys. Astrophys. Fluid Dyn.* **106** (4–5), 392–428.

KING, E.M. & AURNOU, J.M. 2013 Turbulent convection in liquid metal with and without rotation. *Proc. Natl Acad. Sci. USA* **110** (17), 6688–6693.

KING, E.M., STELLMACH, S. & AURNOU, J.M. 2012 Heat transfer by rapidly rotating Rayleigh–Bénard convection. *J. Fluid Mech.* **691**, 568–582.

KING, E.M., STELLMACH, S. & BUFFETT, B. 2013 Scaling behaviour in Rayleigh–Bénard convection with and without rotation. *J. Fluid Mech.* **717**, 449–471.

KING, E.M., STELLMACH, S., NOIR, J., HANSEN, U. & AURNOU, J.M. 2009 Boundary layer control of rotating convection systems. *Nature* **457**, 301–304.

KUNDU, P.K. & COHEN, I.M. 2004 *Fluid Mechanics*. Elsevier Academic Press.

KUNNEN, R.P.J. 2021 The geostrophic regime of rapidly rotating turbulent convection. *J. Turbul.* **22** (4–5), 267–296.

KUNNEN, R.P.J., STEVENS, R.J.A.M., OVERKAMP, J., SUN, C., VAN HEIJST, G.F. & CLERCX, H.J.H. 2011 The role of Stewartson and Ekman layers in turbulent rotating Rayleigh–Bénard convection. *J. Fluid Mech.* **688**, 422–442.

LONG, R.S., MOUND, J.E., DAVIES, C.J. & TOBIAS, S.M. 2020 Scaling behaviour in spherical shell rotating convection with fixed-flux thermal boundary conditions. *J. Fluid Mech.* **889**, A7.

MADONIA, M., GUZMÁN, A.J.A., CLERCX, H.J.H. & KUNNEN, R.P.J. 2021 Velocimetry in rapidly rotating convection: spatial correlations, flow structures and length scales. *Europhys. Lett.* **135** (5), 54002.

MAFFEI, S., KROUSS, M., JULIEN, K. & CALKINS, M. 2021 On the inverse cascade and flow speed scaling behaviour in rapidly rotating Rayleigh–Bénard convection. *J. Fluid Mech.* **913**, A18.

NIEMELA, J.J., SKRBEK, L., SREENIVASAN, K.R. & DONNELLY, R.J. 2000 Turbulent convection at very high Rayleigh numbers. *Nature* **404**, 837–840.

PANDEY, A., KRASNOV, D., SCHUMACHER, J., SAMTANEY, R. & SREENIVASAN, K.R. 2022*a* Similarities between characteristics of convective turbulence in confined and extended domains. *Physica* D **442**, 133537.

PANDEY, A., KRASNOV, D., SREENIVASAN, K.R. & SCHUMACHER, J. 2022*b* Convective mesoscale turbulence at very low Prandtl numbers. *J. Fluid Mech.* **948**, A23.

PANDEY, A. & SREENIVASAN, K.R. 2021 Convective heat transport in slender cells is close to that in wider cells at high Rayleigh and Prandtl numbers. *Europhys. Lett.* **135** (2), 24001.

PANDEY, A. & VERMA, M.K. 2016 Scaling of large-scale quantities in Rayleigh–Bénard convection. *Phys. Fluids* **28** (9), 095105.

PLUMLEY, M. & JULIEN, K. 2019 Scaling laws in Rayleigh–Bénard convection. *Earth Space Sci.* **6** (9), 1580–1592.

SCHEEL, J.D., EMRAN, M.S. & SCHUMACHER, J. 2013 Resolving the fine-scale structure in turbulent Rayleigh–Bénard convection. *New J. Phys.* **15**, 113063.

SCHEEL, J.D. & SCHUMACHER, J. 2017 Predicting transition ranges to fully turbulent viscous boundary layers in low Prandtl number convection flows. *Phys. Rev. Fluids* **2**, 123501.

SCHINDLER, F., ECKERT, S., ZÜRNER, T., SCHUMACHER, J. & VOGT, T. 2022 Collapse of coherent large scale flow in strongly turbulent liquid metal convection. *Phys. Rev. Lett.* **128**, 164501.

SCHMITZ, S. & TILGNER, A. 2010 Transitions in turbulent rotating Rayleigh–Bénard convection. *Geophys. Astrophys. Fluid Dyn.* **104** (5–6), 481–489.

SCHUMACHER, J., GÖTZFRIED, P. & SCHEEL, J.D. 2015 Enhanced enstrophy generation for turbulent convection in low-Prandtl-number fluids. *Proc. Natl Acad. Sci. USA* **112**, 9530–9535.

SCHUMACHER, J. & SREENIVASAN, K.R. 2020 Colloquium: unusual dynamics of convection in the Sun. *Rev. Mod. Phys.* **92**, 041001.

SHISHKINA, O. 2020 Tenacious wall states in thermal convection in rapidly rotating containers. *J. Fluid Mech.* **898**, F1.

SHISHKINA, O. 2021 Rayleigh–Bénard convection: the container shape matters. *Phys. Rev. Fluids* **6**, 090502.

SHRAIMAN, B.I. & SIGGIA, E.D. 1990 Heat transport in high-Rayleigh-number convection. *Phys. Rev.* A **42**, 3650–3653.

SONG, J., SHISHKINA, O. & ZHU, X. 2024 Scaling regimes in rapidly rotating thermal convection at extreme Rayleigh numbers. *J. Fluid Mech.* **984**, A45.

SPRAGUE, M., JULIEN, K., KNOBLOCH, E. & WERNE, J. 2006 Numerical simulation of an asymptotically reduced system for rotationally constrained convection. *J. Fluid Mech.* **551**, 141–174.

STELLMACH, S., LISCHPER, M., JULIEN, K., VASIL, G., CHENG, J.S., RIBEIRO, A., KING, E.M. & AURNOU, J.M. 2014 Approaching the asymptotic regime of rapidly rotating convection: boundary layers versus interior dynamics. *Phys. Rev. Lett.* **113**, 254501.

STEVENS, R., ZHONG, J., CLERCX, H., AHLERS, G. & LOHSE, D. 2009 Transitions between turbulent states in rotating Rayleigh–Bénard convection. *Phys. Rev. Lett.* **103**, 024503.

STEVENS, R.J., CLERCX, H.J. & LOHSE, D. 2013 Heat transport and flow structure in rotating Rayleigh–Bénard convection. *Eur. J. Mech.* B **40**, 41–49.

VERMA, M.K., KUMAR, A. & PANDEY, A. 2017 Phenomenology of buoyancy-driven turbulence: recent results. *New J. Phys.* **19** (2), 025012.

VOGT, T., HORN, S. & AURNOU, J.M. 2021 Oscillatory thermal–inertial flows in liquid metal rotating convection. *J. Fluid Mech.* **911**, A5.

WAGNER, S. & SHISHKINA, O. 2013 Aspect-ratio dependency of Rayleigh–Bénard convection in box-shaped containers. *Phys. Fluids* **25**, 085110.

WEDI, M., VAN GILS, D.P., BODENSCHATZ, E. & WEISS, S. 2021 Rotating turbulent thermal convection at very large Rayleigh numbers. *J. Fluid Mech.* **912**, A30.

WEDI, M., MOTURI, V.M., FUNFSCHILLING, D. & WEISS, S. 2022 Experimental evidence for the boundary zonal flow in rotating Rayleigh–Bénard convection. *J. Fluid Mech.* **939**, A14.

DE WIT, X.M., AGUIRRE GUZMÁN, A.J., MADONIA, M., CHENG, J.S., CLERCX, H.J.H. & KUNNEN, R.P.J. 2020 Turbulent rotating convection confined in a slender cylinder: the sidewall circulation. *Phys. Rev. Fluids* **5**, 023502.

ZHANG, K. & LIAO, X. 2017 *Theory and Modeling of Rotating Fluids: Convection, Inertial Waves and Precession*. Cambridge University Press.

ZHANG, X., ECKE, R.E. & SHISHKINA, O. 2021 Boundary zonal flows in rapidly rotating turbulent thermal convection. *J. Fluid Mech.* **915**, A62.

ZHANG, X., VAN GILS, D.P.M., HORN, S., WEDI, M., ZWIRNER, L., AHLERS, G., ECKE, R.E., WEISS, S., BODENSCHATZ, E. & SHISHKINA, O. 2020 Boundary zonal flow in rotating turbulent Rayleigh–Bénard convection. *Phys. Rev. Lett.* **124**, 084505.

ZHONG, F., ECKE, R.E. & STEINBERG, V. 1993 Rotating Rayleigh–Bénard convection: asymmetric modes and vortex states. *J. Fluid Mech.* **249**, 135–159.

ZHONG, J.-Q. & AHLERS, G. 2010 Heat transport and the large-scale circulation in rotating turbulent Rayleigh–Bénard convection. *J. Fluid Mech.* **665**, 300–333.

ZHONG, J.-Q., STEVENS, R.J.A.M., CLERCX, H.J.H., VERZICCO, R., LOHSE, D. & AHLERS, G. 2009 Prandtl-, Rayleigh-, and Rossby-number dependence of heat transport in turbulent rotating Rayleigh–Bénard convection. *Phys. Rev. Lett.* **102**, 044502.

ZWIRNER, L., TILGNER, A. & SHISHKINA, O. 2020 Elliptical instability and multiple-roll flow modes of the large-scale circulation in confined turbulent Rayleigh–Bénard convection. *Phys. Rev. Lett.* **125**, 054502.